

REPORT DOCUMENTATION PAGE

Form Approved
OMB No. 0704-0188

Public reporting burden for this collection of information is estimated to average 1 hour per response, including the time for reviewing instructions, searching existing data sources, gathering and maintaining the data needed, and completing and reviewing the collection of information. Send comments regarding this burden estimate or any other aspect of this collection of information, including suggestions for reducing this burden, to Washington Headquarters Services, Directorate for Information Operations and Reports, 1215 Jefferson Davis Highway, Suite 1204, Arlington, VA 22202-4302, and to the Office of Management and Budget, Paperwork Reduction Project (0704-0188), Washington, DC 20503.

1. AGENCY USE ONLY (Leave blank)		2. REPORT DATE FEB 1994		3. REPORT TYPE AND DATES COVERED FINAL 09/01/92--12/31/93	
4. TITLE AND SUBTITLE CONTINUUM TRANSIENT AND FROZEN STARTUP BEHAVIOR OF CONVENTIONAL AND GAS- LOADED HEAT PIPES				5. FUNDING NUMBERS C F33615-88-C-2820 PE 62203 PR 3145 TA 20 WU 06	
6. AUTHOR(S) AMIR FAGHRI, PH.D.					
7. PERFORMING ORGANIZATION NAME(S) AND ADDRESS(ES) DEPARTMENT OF MECHANICAL AND MATERIALS ENGINEERING WRIGHT STATE UNIVERSITY DAYTON OH 45435				8. PERFORMING ORGANIZATION REPORT NUMBER	
9. SPONSORING / MONITORING AGENCY NAME(S) AND ADDRESS(ES) AEROPROPULSION AND POWER DIRECTORATE WRIGHT LABORATORY AIR FORCE MATERIEL COMMAND WRIGHT PATTERSON AFB OH 45433-7251				10. SPONSORING / MONITORING AGENCY REPORT NUMBER WL-TR-94-2044	
11. SUPPLEMENTARY NOTES					
12a. DISTRIBUTION / AVAILABILITY STATEMENT APPROVED FOR PUBLIC RELEASE; DISTRIBUTION IS UNLIMITED.				12b. DISTRIBUTION CODE	
13. ABSTRACT (Maximum 200 words) The heat pipe startup process is described physically and mathematically. During most of the heat pipe startup process, the continuum and rarefied vapor flows co-exist along the heat pipe length. A two-region model is thereby proposed in which the vapor flow in the continuum region is modeled by the compressible Navier-Stokes equations, and the vapor flow in the rarefied region is modeled by the self-diffusion model. The two vapor regions are linked with appropriate boundary conditions, and the heat pipe wall, wick and vapor flow are solved as a conjugate problem. Both numerical and analytical solutions for the entire heat pipe startup process from the frozen state are compared with the corresponding experimental data with good agreement.					
DTIC QUALITY INSPECTED 3					
14. SUBJECT TERMS HEAT PIPE, TRANSIENT, FROZEN STARTUP, GAS LOADED				15. NUMBER OF PAGES 106	
				16. PRICE CODE	
17. SECURITY CLASSIFICATION OF REPORT UNCLASSIFIED		18. SECURITY CLASSIFICATION OF THIS PAGE UNCLASSIFIED		19. SECURITY CLASSIFICATION OF ABSTRACT UNCLASSIFIED	
20. LIMITATION OF ABSTRACT UL					

Contents

Accession For		
NTIS	CRA&I	<input checked="" type="checkbox"/>
DTIC	TAB	<input type="checkbox"/>
Unannounced		<input type="checkbox"/>
Justification		
By		
Distribution /		
Availability Codes		
Dist	Avail and/or Special	
A-1		

List of Figures	v
List of Tables	ix
List of Symbols	xi

1 NUMERICAL MODEL OF FROZEN STARTUP OF HIGH-TEMPERATURE

HEAT PIPES	1
1.1 SUMMARY	1
1.2 INTRODUCTION	2
1.3 RAREFIED VAPOR FLOW REGION	3
1.4 CONTINUUM VAPOR FLOW REGION	5
1.5 HEAT PIPE WALL AND WICK	6
1.6 BOUNDARY CONDITIONS	8
1.7 NUMERICAL MODELING AND PREDICTIONS	10

2 CLOSED-FORM ANALYTICAL MODEL OF FROZEN STARTUP

Table of Contents

OF HIGH-TEMPERATURE HEAT PIPES	25
2.1 SUMMARY	25
2.2 INTRODUCTION	26
2.3 ANALYTICAL SOLUTION	28
2.4 FROZEN-STARTUP LIMITATION	40
 3 TRANSIENT TWO-DIMENSIONAL GAS-LOADED HEAT PIPE	
ANALYSIS	48
3.1 SUMMARY	48
3.2 INTRODUCTION	49
3.3 MATHEMATICAL MODELING	51
3.3.1 Vapor Space	51
3.3.2 Wall and Wick	55
3.3.3 Boundary Conditions	56
3.3.4 Initial Conditions	60
3.4 NUMERICAL METHODOLOGY	60
3.5 RESULTS AND DISCUSSION	62
3.6 CONCLUSIONS	79
 4 REFERENCES	83

List of Figures

1.1	Schematic of continuum and rarefied vapor regions and interfacial grids	11
1.2	Heat pipe frozen startup in the early stages (Case 24a, evaporator 2 active, $Q = 60$ W): (a) Outer wall temperature compared with experimental data of Faghri et al. (1991a); (b) Vapor Mach number; (c) Vapor density	14
1.3	Outer wall temperatures with different accommodation coefficients at $t = 675$ s for Case 24a	16
1.4	Outer wall temperatures compared with experimental data for Cases 11a-11f	17
1.5	Outer wall temperatures compared with experimental data given by Ponnappan (1989) for $Q = 289.6$ W	20
1.6	Comparison of centerline vapor and wall temperatures for Case 11a .	22
1.7	Axial vapor Mach number for Cases 11a-11f	23
2.1	Description of the flat-front startup model	29

List of Figures

2.2	Analytical wall temperatures compared with experimental data for Case 13a	36
2.3	Analytical wall temperatures compared with experimental data given by Ponnappan (1989) for $Q = 289.6$ W	38
2.4	Analytical wall temperatures compared with experimental data and numerical solution for Case 11a	39
2.5	Description of the frozen-startup limit	41
2.6	Description of the criterion for the frozen-startup limit	43
3.1	Gas-loaded heat pipe configuration and coordinate system.	52
3.2	Numerical simulation of the high-temperature heat pipe (Case 1): (a) Vapor temperature contours; (b) Vapor velocity vectors in the r - z plane; (c) Vapor pressure contours.	65
3.3	Temperature profiles for conventional heat pipe with $Q_{in} = 515$ W (Case 1): (a) Transient wall temperature profile; (b) Transient centerline temperature profile.	67
3.4	Vapor flow dynamics for conventional heat pipe with $Q_{in} = 515$ W (Case 1): (a) Transient centerline pressure profile; (b) Transient centerline axial velocity profile.	69

List of Figures

3.5	Temperature profiles for gas-loaded heat pipe with $Q_{in} = 451$ W (Case 2): (a) Transient wall temperature profile; (b) Transient centerline temperature profile.	70
3.6	Vapor-gas dynamics for the gas-loaded heat pipe with $Q_{in} = 451$ W (Case 2): (a) Transient centerline gas density profile; (b) Transient centerline axial velocity profile.	71
3.7	Numerical simulation of the gas-loaded high-temperature heat pipe (Case 3): (a) Vapor temperature contours; (b) Noncondensable gas density profiles; (c) Vapor velocity vectors in the r - z plane; (d) Vapor pressure contours.	72
3.8	Temperature profiles for the gas-loaded heat pipe with $Q_{in} = 258$ W (Case 3): (a) Transient wall temperature profile; (b) Transient centerline temperature profile.	74
3.9	Vapor-gas dynamics for the gas loaded heat pipe with $Q_{in} = 258$ W (Case 3): (a) Transient centerline gas density profile; (b) Transient centerline axial velocity profile.	75
3.10	Temperature profiles for the gas-loaded heat pipe with a pulsed heat input of $Q_{in} = 258$ to 306 W (Case 3): (a) Transient wall temperature profile; (b) Transient centerline temperature profile.	77

- 3.11 Vapor-gas dynamics for the gas-loaded heat pipe with a pulsed heat input of $Q_{in} = 258$ to 306 W (Case 3): (a) Transient centerline gas density profile; (b) Transient centerline axial velocity profile. 78
- 3.12 Temperature profiles for the gas-loaded heat pipe with a pulsed heat input of $Q_{in} = 258$ to 451 W (Case 4): (a) Transient wall temperature profile; (b) Transient centerline temperature profile. 80
- 3.13 Vapor-gas dynamics for the gas-loaded heat pipe with a pulsed heat input of $Q_{in} = 258$ to 451 W (Case 4): (a) Transient centerline gas density profile; (b) Transient centerline axial velocity profile. 81

List of Tables

1.1	Summary of the mathematical models and boundary conditions for the analysis of startup from the frozen state	9
1.2	Design summary of the high-temperature heat pipe with multiple heat sources	13
1.3	Design summary of the gas-loaded high-temperature double-wall artery heat pipe (Ponnappan, 1989)	19
3.1	Operating conditions for various cases	63
3.2	Heat pipe geometry and parameters	64

FOREWORD

The information in this report was assembled for contract #F33615-88-C-2820 with the Aero Propulsion and Power Directorate, Wright Laboratory and NASA Lewis Research Center as the sponsoring agencies. This is the fourth and last annual report on this contract. The other three reports were WL-TR-91-2036, WRDC-TR-90-2031 and WRDC-TR-89-2077. It should be noted that more than 30 journal publications were produced from this contract. The work was carried out at the Department of Mechanical and Materials Engineering at Wright State University.

During 1992-93, three major tasks were performed as outlined in the Table of Contents. The various tasks dealt with the frozen startup of high-temperature heat pipes, as well as transient operation of gas-loaded heat pipes. Five journal publications were produced from the present work. Three graduate research assistants were involved in the preparation of this work. Dr. Won Chang from Wright Laboratory was the technical supervisor for this contract and the author is grateful to him for his discussions and comments. Support from Dr. Jerry Beam and Dr. Tom Mahefkey from Wright Laboratory and Mr. Jim Calogeras, Mr. Al Juhasz, Mr. Karl Baker, and Mr. Ron Sovie from NASA Lewis Research Center is greatly appreciated.

List of Symbols

NOMENCLATURE

A	cross-sectional area, m^2
c	specific heat, $\text{J}/(\text{kg}\cdot\text{K})$
C	heat capacity per unit length, $\text{J}/(\text{m}\cdot\text{K})$
c_p	specific heat at constant pressure, $\text{J}/(\text{kg}\cdot\text{K})$
C_t	total thermal capacity of the heat pipe, J/K
c_v	specific heat at constant volume, $\text{J}/(\text{kg}\cdot\text{K})$
D	vapor space diameter, m
D_d	self-diffusion coefficient, m^2/s
D_v	coefficient of self-diffusion, m^2/s
D_{gv}	mass diffusion coefficient, m^2/s
f	skin friction coefficient, $2\tau_w/\rho\bar{w}^2$
G	vapor mass flux due to diffusion, $\text{kg}/(\text{m}^2\cdot\text{s})$
h	convective heat transfer coefficient, $\text{W}/(\text{m}^2\cdot\text{K})$
H	latent heat due to melting or freezing, J/kg
h_{fg}	latent heat of evaporation J/kg
k	thermal conductivity, $\text{W}/(\text{m}\cdot\text{K})$
K	permeability, m^2
K_p	density correction coefficient, s^2/m^2
K'	ratio of specific heats, c_p/c_v

List of Symbols

Kn	Knudsen number, λ/D
l	hot zone length, m
L	length, m
m	mass, kg
Ma	Mach number, $\bar{w}\sqrt{K'p/\rho_v}$
M	molecular weight, kg/kmol
\dot{m}	mass flow rate, kg/s
\dot{m}_g''	mass flux at the liquid-vapor interface, kg/(m ² -s)
n	normal direction of the liquid-vapor interface
p	pressure, N/m ²
p_0	reference pressure, N/m ²
p'	pressure correction, N/m ²
q	heat flux, W/m ²
Q	heat input, W
q_{so}	heat source, W/m ²
r	radial coordinate, m
R	thermal resistance, K/W
R_g	gas constant, J/(kg-K)
R_i	wick-wall interface radius, m
R_o	outer pipe wall radius, m

List of Symbols

R_o	outer surface radius, m
R_u	universal gas constant, J/(mol-K)
R_v	vapor space radius, m
R_w	wick-wall interface radius, m
R	universal gas constant, N-m/(kmol-K)
Re	Reynolds number, $\bar{w}D/\nu$
s	source term
S	surface area, m ²
t	time, s
T	temperature, K
T_{aw}	average hot zone temperature, K
T_h	hot zone temperature at the evaporator end cap, K
$T_{i,c}$	interfacial temperature on the continuum vapor flow side, K
$T_{i,r}$	interfacial temperature on the rarefied vapor flow side, K
T_i	wall-wick interfacial temperature, K
T_{mel}	melting temperature, K
T_{tr}	transition vapor temperature, K
T_0	reference temperature, K
v	radial velocity, m/s
v	radial velocity component, m/s

List of Symbols

v^*	radial velocity based on guessed pressure, m/s
V_t	total volume of the heat pipe, m ³
v_δ	radial blowing/suction velocity at the wall, m/s
\vec{V}	net velocity vector, m/s
w	axial velocity component, m/s
w^*	axial velocity based on guessed pressure, m/s
\bar{w}	mean axial velocity, m/s
$w_{i,r}$	interfacial axial velocity on the rarefied vapor flow side, m/s
W	circumferential length, m
W_i	liquid-solid interface axial velocity, m/s
z	axial coordinate, m

Greek symbols

α	thermal diffusivity of the vapor, m ² /s, or accommodation coefficient
δ_l	wick thickness, m
δ_w	wall thickness
δT	one-half phase-change temperature range, K
ΔT	temperature drop across hot zone, $T_h - T_{tr}$, K
Δz	control volume size in axial direction, m

List of Symbols

ϵ	emissivity, or maximum energy of attraction between a pair of molecules
κ	Boltzmann constant, J/K
λ	mean free path, m
μ	dynamic viscosity, kg/(m-s)
ν	kinematic viscosity, m ² /s
ρ	density, kg/m ³
$\rho_{i,c}$	interfacial density on the continuum vapor side, kg/m ³
ρ^*	guessed density, kg/m ³
ρ'	density correction, kg/m ³
σ	Stefan-Boltzmann constant, W/(m ² -K ⁴), or collision diameter, Å
σ_z	normal stress, N/m ²
τ	time constant, s
τ_w	wall shear stress, N/m ²
τ_0	characteristic time, s
φ	porosity
Φ	viscous dissipation
Φ	viscous dissipation term
Ω_D	collision integral for mass diffusion

List of Symbols

Subscripts

<i>a</i>	adiabatic or active
<i>av</i>	average
<i>c</i>	condenser
<i>cond</i>	conduction
<i>conv</i>	convection
<i>e</i>	evaporator
<i>eff</i>	effective
<i>g</i>	gas
<i>i</i>	initial
<i>in</i>	into the interface
<i>l</i>	liquid
<i>le</i>	wick region where the working fluid is in the liquid state
<i>me</i>	wick region where the working fluid is in the mushy state
<i>r</i>	in the radial direction
<i>rad</i>	radiation
<i>s</i>	wick structure material
<i>sat</i>	saturation
<i>se</i>	wick region where the working fluid is in the solid state
<i>so</i>	source

List of Symbols

t	total
tr	transition quantity
v	vapor
w	wall
w	wall or wick
ws	wick structure material
z	in the axial direction
δ	liquid-vapor interface
0	reference
∞	ambient
δ	liquid-vapor interface

Superscript

$-$	Mass fraction weighted quantity
-----	---------------------------------

NUMERICAL MODEL OF FROZEN STARTUP OF HIGH-TEMPERATURE HEAT PIPES

1.1 SUMMARY

Continuum and rarefied vapor flows co-exist along the heat pipe length for most of the startup period. A two-region model is proposed in which the vapor flow in the continuum region is modeled by the compressible Navier-Stokes equations, and the

vapor flow in the rarefied region is simulated by a self-diffusion model. The two vapor regions are linked with appropriate boundary conditions, and the heat pipe wall, wick and vapor flow are solved as a conjugate problem. The numerical solutions for the entire heat pipe startup process from the frozen state are compared with the corresponding experimental data with good agreement.

1.2 INTRODUCTION

Due to the complex heat transfer phenomena occurring within a heat pipe, numerical models are normally used to perform a detailed study of the frozen startup period. Examples of previous works that have developed numerical models include Chang and Colwell (1985), Costello et al. (1987), Hall and Doster (1990), Jang et al. (1990), and Cao and Faghri (1993a). Jang et al. (1990) described the different startup periods, and the general mathematical formulation for each period was given. In an attempt to solve the conservation equations, the effect of the liquid flow in the porous wick structure was neglected, and the vapor flow was simulated with a one-dimensional model. In the initial stage of the simulation, the liquid-vapor interface was assumed to be adiabatic, and only the heat conduction in the wall and the melting in the wick was considered. In the transient continuum flow stage, the vapor was assumed to be in a continuum flow state. An effort to couple the continuum vapor flow with the wick and wall was made, but the coupling was apparently not completed, and the

linkage between the two stages was not considered. Only the model by Cao and Faghri (1993a) examined the entire heat pipe startup process from the early free-molecular vapor condition to the final steady-state operation. The closed-form analytical model by Cao and Faghri (1992) also determined the frozen startup characteristics of high-temperature heat pipes. The numerical and analytical models of Cao and Faghri (1992, 1993a) are described in detail in this section.

Cao and Faghri (1993a) proposed a complete two-dimensional numerical model which split the heat pipe into two regions: continuum and rarefied flows. In the continuum flow region, the mass, momentum, and energy conservation equations were solved. In the rarefied flow region, the self-diffusion model given by Cao and Faghri (1993b) was used. The two regions were coupled with appropriate boundary conditions to model the entire heat pipe as a conjugate problem. This model predicted the transient and steady performance characteristics of a high-temperature heat pipe started from the frozen state.

1.3 RAREFIED VAPOR FLOW REGION

In the early stages of frozen startup, the vapor pressure and density are extremely low. Therefore, the vapor is in the rarefied state, which is somewhat different than that in the continuum state. Also, a very large vapor density gradient exists in the axial direction of the heat pipe. Therefore, the axial motion of the vapor is caused

by molecular diffusion. The rarefied vapor flow can be simulated by a self-diffusion model, where self-diffusion refers to the interdiffusion of particles of the same species due to the density gradient. The conservation of mass and energy equations for a differential cylindrical control volume are

Mass self-diffusion:

$$\frac{\partial \rho}{\partial t} - \frac{\partial}{\partial z} \left(D_v \frac{\partial \rho}{\partial z} \right) - \frac{1}{r} \frac{\partial}{\partial r} \left(r D_v \frac{\partial \rho}{\partial r} \right) = 0 \quad (1.1)$$

Energy:

$$\frac{\partial}{\partial t} (\rho c_v T) + \frac{1}{r} \frac{\partial}{\partial r} (G_r c_p r T) + \frac{\partial}{\partial z} (G_z c_p T) = \frac{1}{r} \frac{\partial}{\partial r} \left(r k_v \frac{\partial T}{\partial r} \right) + \frac{\partial}{\partial z} \left(k_v \frac{\partial T}{\partial z} \right) \quad (1.2)$$

where the mass fluxes G_r and G_z are

$$G_r = \rho v = -D_v \frac{\partial \rho}{\partial r}, \quad G_z = \rho w = -D_v \frac{\partial \rho}{\partial z} \quad (1.3)$$

D_v is the coefficient of self-diffusion, which is given by the relation based on the Chapman-Enskog kinetic theory (Hirschfelder et al., 1966).

$$D_v = 2.628 \times 10^{-7} \frac{\sqrt{T^3/M}}{p \sigma^2 \Omega_D (\kappa T / \epsilon)} \quad (1.4)$$

where p is the pressure in atmospheres, σ is the collision diameter in Å, ϵ is the maximum energy of attraction between a pair of molecules, κ is the Boltzmann constant,

M is the molecular weight, and Ω_D is the collision integral for mass diffusion. The heat dissipation has been neglected due to the low vapor temperature and small vapor viscosity during the frozen startup period.

1.4 CONTINUUM VAPOR FLOW REGION

The vapor flow within heat pipes has been studied previously using experimental, analytical, and numerical methods. Wageman and Guevara (1960) simulated an evaporator by injecting air through a porous pipe in order to study the transition to turbulence. Their experimental results closely matched the laminar flow theory by Yuan and Finkelstein (1956), even for axial Reynolds numbers up to 10^5 , where turbulence should have been well established. Bowman and Hitchcock (1989) studied a simulated heat pipe by injecting and extracting air through a porous pipe. It was found that the vapor flow was always laminar in the evaporator, while it may become turbulent in the condenser above Reynolds numbers of 1.2×10^4 . During the frozen startup process, the axial vapor velocity can be supersonic, but the axial Reynolds number is relatively small due to the low vapor densities of liquid-metal working fluids. Faghri et al. (1991b) showed that the axial Reynolds number was less than 500. Therefore, the continuum vapor flow in the heat pipe can be assumed to be laminar along the entire heat pipe length.

1.5 HEAT PIPE WALL AND WICK

The heat transfer through the heat pipe wall is by conduction. The change of phase of the frozen working fluid must be considered in the wick structure, which is assumed to be isotropic and homogeneous. The phase-change model by Cao and Faghri (1990b) was employed by Cao and Faghri (1993a, 1993b), which is a fixed-grid formulation having the advantage of eliminating time-step and grid-size limitations. In this analysis, the effect of the liquid flow in the wick on the temperature distribution has been neglected. This is due to the fact that the wick is usually very thin, the thermal conductivity of the liquid metal is high, and heat conduction is the dominant transport mechanism in the wick structure. The validity of this conduction model in the wick was also documented by Ivanovskii et al. (1982) and Dunn and Reay (1982). The conservation of energy equation below is also applicable to the entire frozen startup process.

$$\frac{\partial}{\partial t}(\rho_{\text{eff}}CT) = \frac{\partial}{\partial z} \left(k_{\text{eff}} \frac{\partial T}{\partial z} \right) + \frac{1}{r} \frac{\partial}{\partial r} \left(k_{\text{eff}} r \frac{\partial T}{\partial r} \right) - \frac{\partial}{\partial t}(\rho_{\text{eff}}S) \quad (1.5)$$

The coefficients $C = C(T)$, $S = S(T)$, and $k_{\text{eff}} = k_{\text{eff}}(T)$ are given by

$$C(T) = \begin{cases} c_{se}, & (T < T_{mel} - \delta T) & \text{(solid phase)} \\ c_{me} + H/2\delta T, & (T_{mel} - \delta T \leq T \leq \delta T + T_{mel}) & \text{(mushy phase)} \\ c_{le}, & (T > T_{mel} + \delta T) & \text{(liquid phase)} \end{cases} \quad (1.6)$$

$$S(T) = \begin{cases} c_{se}(\delta T - T_{mel}), & (T < T_{mel} - \delta T) \\ c_{me}\delta T + H/2 - (c_{me} + H/2\delta T)T_{mel}, & (T_{mel} - \delta T \leq T \leq \delta T + T_{mel}) \\ c_{se}\delta T + H - c_{le}T_{mel}, & (T > T_{mel} + \delta T) \end{cases} \quad (1.7)$$

$$k_{eff}(T) = \begin{cases} k_{se}, & (T < T_{mel} - \delta T) \\ k_{se}(k_{le} - k_{se})(T - T_{mel} + \delta T)/2\delta T, & (T_{mel} - \delta T \leq T \leq \delta T + T_{mel}) \\ k_{le}, & (T > T_{mel} + \delta T) \end{cases} \quad (1.8)$$

where

$$\rho_{eff} = \varphi\rho_l + (1 - \varphi)\rho_{ws}, \quad c_{se} = \varphi c_s + (1 - \varphi)c_{ws}$$

$$c_{le} = \varphi c_l + (1 - \varphi)c_{ws}, \quad c_{me} = (c_{se} + c_{le})/2$$

For a wrapped screen wick, k_{se} and k_{le} are calculated using the equation given in

Section 3.

$$k_{se} = \frac{k_s [(k_s + k_{ws}) - (1 - \varphi)(k_s - k_{ws})]}{[(k_s + k_{ws}) + (1 - \varphi)(k_s - k_{ws})]} \quad (1.9)$$

$$k_{le} = \frac{k_\ell [(k_\ell + k_{ws}) - (1 - \varphi)(k_\ell - k_{ws})]}{[(k_\ell + k_{ws}) + (1 - \varphi)(k_\ell - k_{ws})]} \quad (1.10)$$

1.6 BOUNDARY CONDITIONS

A complete summary of the boundary conditions applicable to the frozen startup of high-temperature heat pipes can be found in Table 1.1. After the melting interface reaches the wick-vapor interface, $r = R_v$, evaporation or condensation takes place. The relation for the interface mass flux is

$$\dot{m}_s'' = -\rho_s v_s = \left(\frac{2\alpha}{2 - \alpha} \right) \sqrt{\frac{M}{2\pi R_u}} \left(\frac{p_\ell^*}{\sqrt{T_\ell}} - \frac{p_v}{\sqrt{T_v}} \right) \quad (1.11)$$

where $\dot{m}_s > 0$ for evaporation, < 0 for condensation, and α is the accommodation coefficient. p_ℓ^* is the equilibrium saturation pressure corresponding to the liquid temperature T_ℓ , and can be calculated using the Clausius-Clapeyron equation.

$$p_\ell^* = p_0 \exp \left[-\frac{h_{fg}}{R_g} \left(\frac{1}{T_\ell} - \frac{1}{T_0} \right) \right] \quad (1.12)$$

p_0 and T_0 are the reference pressure and temperature. Sukhatme and Rohsenow (1966) showed that α may change from 0.1 to 1.0, according to the surface condition.

As was previously mentioned, a two-region model for the vapor flow in the heat pipe was employed. The continuum and rarefied regions are coupled at the

1.1 Summary of the mathematical models and boundary conditions for the analysis of startup from the frozen state

Heat Pipe Regions	Description of Governing Equations and Boundary Conditions in Different Regions in Radial Direction (All of These Regions were Solved as a Conjugate Problem)	
Wall	<p>Boundary conditions: Outer wall surface $r = R_o$: $k_w \frac{\partial T}{\partial r} = q_e \quad (0 \leq z \leq L_e)$ $\frac{\partial T}{\partial r} = 0 \quad [L_e < z < (L_e + L_d)]$ $-k_w \frac{\partial T}{\partial r} = \sigma \epsilon (T_w^4 - T_{\infty}^4) \quad [(L_e + L_d) \leq z \leq L_t]$ Wall-wick interface, $r = R_w$: $k_w \frac{\partial T}{\partial r} = k_{sc} \frac{\partial T}{\partial r}$ (when working fluid is in solid state), $k_w \frac{\partial T}{\partial r} = k_{lc} \frac{\partial T}{\partial r}$ (when working fluid is in liquid state) Evaporator and condenser end caps, $z = 0$ and L_t: $\frac{\partial T}{\partial z} = 0$</p>	
Wick	<p>Boundary conditions: Wick-vapor interface, $r = R_v$: Evaporator and condenser end caps, $z = 0$ and L_t: $\frac{\partial T}{\partial z} = 0$</p>	
Vapor	Continuum Vapor Flow Region	Rarefied Vapor Flow Region
	<p>Boundary conditions: Heat pipe centerline, $r = 0$: $\frac{\partial w}{\partial r} = v = \frac{\partial T}{\partial r} = 0$ Evaporator and condenser end caps, $z = 0$ and L_t: $v = w = \frac{\partial T}{\partial z} = 0$ Continuum-rarefied interface[†]: $w = w_{i,r}$, $\frac{\partial w}{\partial z} = 0$, $T = T_{i,r}$</p>	<p>Boundary conditions: Heat pipe centerline, $r = 0$: $\frac{\partial T}{\partial r} = \frac{\partial \rho}{\partial r} = 0$ Evaporator and condenser end caps, $z = 0$ and L_t: $\frac{\partial \rho}{\partial z} = \frac{\partial T}{\partial z} = 0$ Continuum-rarefied interface[‡]: $\rho = \rho_{i,c}$, $T = T_{i,c}$</p>

[†] $w_{i,r}$ and $T_{i,r}$ are interfacial values from the rarefied vapor solution.

[‡] $\rho_{i,c}$ and $T_{i,c}$ are interfacial values from the continuum vapor solution.

continuum-rarefied interface, which is assumed to be planar. The two regions and the interfacial grids are shown in Fig. 1.1.

It is essential to maintain the mass balance across the interface at each time step. The boundary conditions at the continuum-rarefied interface are

$$w = w_{i,r}, \quad \frac{\partial v}{\partial z} = 0, \quad T = T_{i,r} \quad (\text{continuum vapor flow}) \quad (1.13)$$

$$\rho = \rho_{i,c}, \quad T = T_{i,c} \quad (\text{rarefied vapor flow}) \quad (1.14)$$

where $w_{i,r}$ and $T_{i,r}$ are the interfacial axial vapor velocity and temperature on the rarefied vapor flow side, and are obtained from the rarefied vapor flow solution. $\rho_{i,c}$ and $T_{i,c}$ are the interfacial vapor density and temperature on the continuum vapor flow side, and are obtained from the continuum vapor flow solution.

1.7 NUMERICAL MODELING AND PREDICTIONS

The conjugate heat transfer and flow problem was solved using the control-volume, finite-difference technique with the SIMPLE algorithm. The details of the numerical scheme are given by Cao and Faghri (1993a).

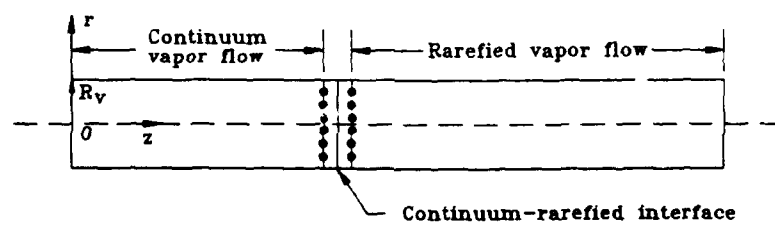


Figure 1.1: Schematic of continuum and rarefied vapor regions and interfacial grids

The frozen startup model was used to simulate the early startup period for the experimental heat pipe studied by Faghri et al. (1991a, 1991b). The multiple-evaporator sodium stainless-steel heat pipe had a vapor space radius $R_v = 10.75$ mm, wrapped screen wick thickness $\delta_l = 0.456$ mm, and pipe wall thickness $\delta_w = 2.15$ mm. The details of the heat pipe and experimental setup are given in Table 1.2. Figure 1.2(a) shows the comparison between the numerical and experimental outer wall temperatures for the early startup period (Case 24a, Faghri et al., 1991a). As can be seen, the agreement is quite good in the early startup period. The accommodation coefficient was specified to be $\alpha = 0.3$, and the phase-change temperature range was set to $2\delta T = 1.0$ K to simulate the phase-change occurring at a single temperature. The melting front reached the wick-vapor interface in the evaporator region quickly (about 40 s). This means that the startup period 2 is very short.

The vapor Mach number for this case is shown in Fig. 1.2(b). Since the active evaporator was located away from the evaporator end cap, the vapor flows both toward the condenser and the evaporator end caps. Very early in the startup, the vapor density was very low, and the Mach number was high. As vapor accumulated in the active heater section due to evaporation, the vapor velocity decreased to the subsonic state ($Ma < 1$) due to the larger vapor density. Away from the active heater, the vapor density was very low, and the vapor velocity reached the supersonic state in both directions. The axial vapor density distribution is shown in Fig. 1.2(c).

Table 1.2: Design summary of the high-temperature heat pipe with multiple heat sources

Container material	304L Stainless Steel
Wick material	304 Stainless Steel
End cap material	304L Stainless Steel
Length	1000 mm
Container o.d.	26.7 mm
Container i.d.	22.4 mm
End cap thickness	3.175 mm
Screen mesh number	100 mesh (3.94 mm^{-1})
Screen wire diameter	0.114 mm
Screen wick thickness	0.456 mm
Vapor core diameter	21.5 mm
Working fluid	sodium
Fluid charge	30, 43 g
Evaporator length*	(4) @ 53.0 mm each
Transport length	188 mm
Condenser length**	292 mm

(*)=Evaporators separated by 90 mm adiabatic sections with a 20 mm adiabatic section between the evaporator end cap and evaporator 1

(**)=20 mm adiabatic section between the condenser and the condenser end cap

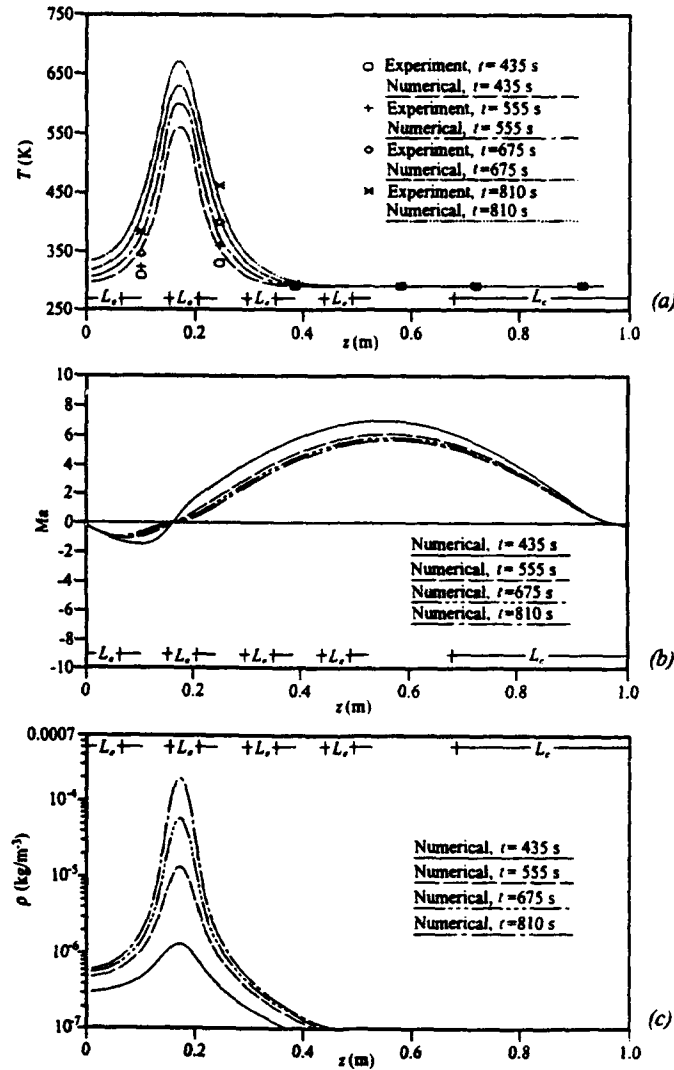


Figure 1.2: Heat pipe frozen startup in the early stages (Case 24a, evaporator 2 active, $Q = 60$ W): (a) Outer wall temperature compared with experimental data of Faghri et al. (1991a); (b) Vapor Mach number; (c) Vapor density

Although the density in the active heater region increased significantly with time, very large density gradients existed in both directions, and the density was very low outside the active evaporator region. Solving eqn. () for the vapor density when continuum flow is established results in $\rho_v \geq 3.3 \times 10^{-4} \text{ kg/m}^3$. From Fig. 1.2(c), it can be seen that continuum flow is reached after 810 s only in the active heater section, while the vapor flow in the rest of the heat pipe is in the rarefied state.

As discussed in Section 2, α may change significantly depending on the surface condition, and there is little information available concerning its value for the wick-vapor interface of a heat pipe. The influence of α on the numerical simulation was examined by running Case 24a again with different values of α , as shown in Fig. 1.3. As can be seen, the numerical results for the outer wall temperature are insensitive to α . Since the wall temperature depends on the interfacial mass flux \dot{m}_g'' , which in turn depends on both α and the pressure difference between the wick-vapor interface and the vapor flow, a larger value of α resulted in a higher vapor pressure and reduced the pressure difference between the wick-vapor interface and the vapor flow. As a result, the two factors offset each other, so the interfacial mass flux remained relatively constant.

Figure 1.4 compares the numerical and experimental outer wall temperatures during all of the frozen startup periods for Cases 11a-11f (Faghri et al., 1991a) with evaporator 1 active, which is closest to the evaporator end cap. The agreement

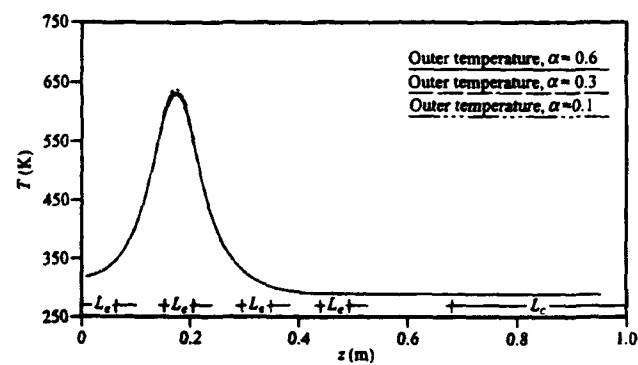


Figure 1.3: Outer wall temperatures with different accommodation coefficients at $t = 675$ s for Case 24a

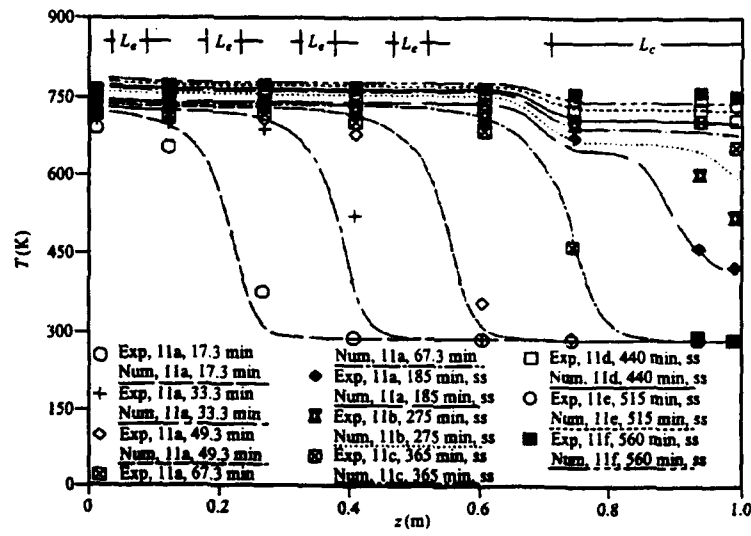


Figure 1.4: Outer wall temperatures compared with experimental data for Cases 11a-11f

between the numerical solutions and the experimental data is generally good. The total heat inputs in the different cases were maintained at different levels in the active evaporator and incremented from 311 W (Case 11a) to 598 W (Case 11f). The corresponding power outputs at the condenser were 119 W (Case 11a) and 298 W (Case 11f). The hot zone moved from the active evaporator down the length of the heat pipe with time. At $t = 185$ min, which corresponds to the steady state for Case 11a, the hot zone reached the condenser section, but the low heat input prevented the hot zone from reaching the condenser end cap. At $t > 185$ min, the heat input was increased to the higher level in Case 11b, and the wall temperature increased. At the heat input corresponding to Case 11c, the hot zone filled the heat pipe completely, and continuum vapor flow was established along the entire heat pipe length. Cases 11a-11c covered the frozen startup process. After Case 11c, the performance is the transient heat pipe operation without phase change from the frozen state. For the numerical results at the steady state, the total heat output at the condenser was within 1.5% of the input at the evaporator in all cases.

The double-wall artery sodium heat pipe studied by Ponnappan (1989) was then simulated. The heat pipe was 2 m in length, with a vapor radius of $R_v = 6.35$ mm, an outer wall radius of $R_o = 11.1$ mm, and a stainless steel wall of thickness $\delta_w = 1.65$ mm. The details of the experimental setup are given in Table 1.3. Figure 1.5 shows the comparison between the numerical and experimental outer wall

Table 1.3: Design summary of the gas-loaded high-temperature double-wall artery heat pipe (Ponnappan, 1989)

Outer tube, inner tube, end caps	304 Stainless steel
Screen wick material	304 Stainless steel
Fill valve	Stainless steel bellows valve with stellite tip stem
Working fluid	sodium
Noncondensable gas	argon
Temperature range	400 to 850°C
Initial temperature	25°C
Heat transport capacity	1800 W at 800°C
Effective length	1.388 m
Total length	2.03 m
Evaporator/adiabatic/condenser	0.375/0.745/0.91 m
Overall diameter	2.22×10^{-2} m
Vapor core diameter	1.27×10^{-2} m
Fluid charge	92.04 g

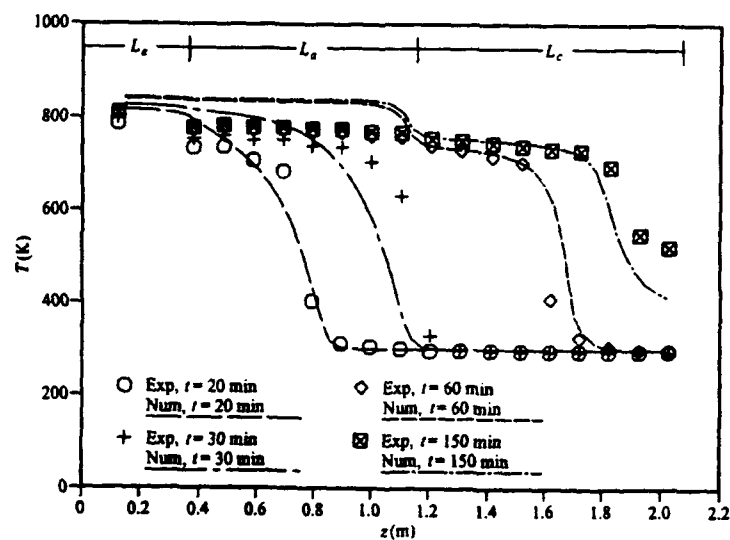


Figure 1.5: Outer wall temperatures compared with experimental data given by Pon-
nappan (1989) for $Q = 289.6$ W

temperatures for a heat rate of $Q = 289.6$ W. Again, the agreement is generally good.

Figure 1.6 shows a comparison between the numerical vapor and wall temperatures for Case 11a. For most of the previous frozen startup studies, the wall temperatures were obtained from experimental measurements, and the vapor temperatures were assumed to be of the same magnitude and trend as the wall temperatures. This is not entirely correct, however, especially in the slope region, as shown in Fig. 1.6. The vapor temperature front is always steeper and is located close to the middle of the slope region of the wall temperature distribution. In order for the hot zone to move forward, heat must be supplied by the vapor to the slope region to increase the wall and wick temperature by condensation in that region. Therefore, a large temperature difference between the wall and vapor is required.

Figure 1.7 shows the axial Mach number along the heat pipe for Cases 11a-11f. The Mach number increased in the evaporator, decreased close to the continuum-rarefied interface, and then increased again in the rarefied region before dropping to zero near the condenser end cap. In the evaporator, the Mach number began to rise due to evaporation at the wick-vapor interface. After the exit of the evaporator, the axial vapor mass flow rate decreased due to condensation. However, the vapor density also decreased significantly in this region. The rate at which the density decreased exceeded the decrease of the axial mass flux due to condensation. Therefore, the vapor velocity and Mach number increased further. When the vapor approached the

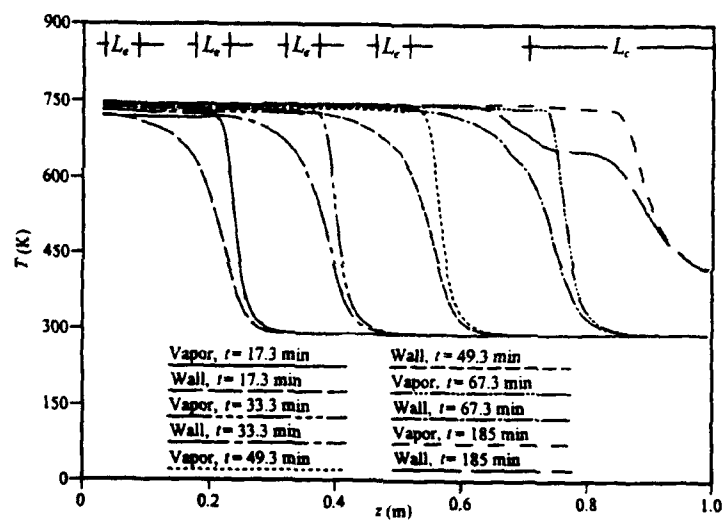


Figure 1.6: Comparison of centerline vapor and wall temperatures for Case 11a

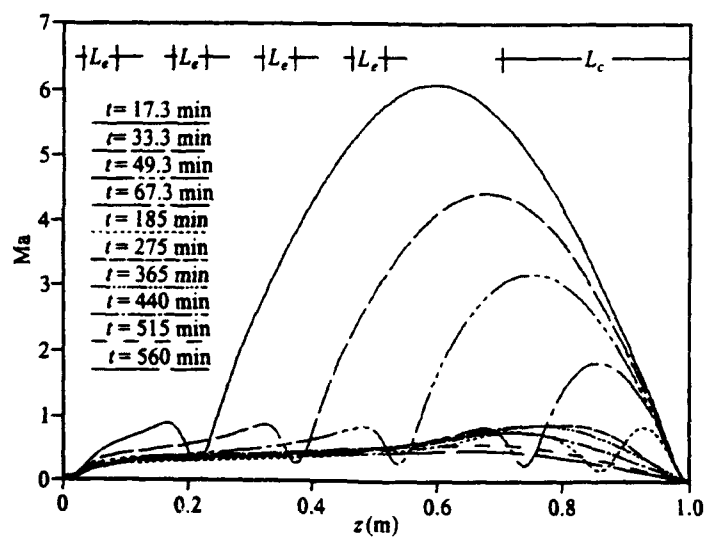


Figure 1.7: Axial vapor Mach number for Cases 11a-11f

hot zone front of the wall temperature, intense condensation occurred. The Mach number decreased to a much lower value before entering the rarefied region. The very large Mach number in the rarefied flow is solely due to the extremely low vapor density. Although the vapor velocity is very high, the mass flux is very low.

CLOSED-FORM ANALYTICAL MODEL OF FROZEN STARTUP OF HIGH-TEMPERATURE HEAT PIPES

2.1 SUMMARY

The previous numerical and experimental studies indicate that the high temperature heat pipe startup process is characterized by a moving hot zone with relatively sharp fronts. Based on the above observation, a flat-front model for an approximate

analytical solution is proposed. A closed-form solution related to the temperature distribution in the hot zone and the hot zone length as a function of time are obtained. The analytical results agree well with the corresponding experimental data, and provide a quick prediction method for the heat pipe startup performance. Finally, a heat pipe limitation related to the frozen startup process is identified, and an explicit criterion for the high temperature heat pipe startup is derived. The frozen startup limit identified in this report provides a fundamental guidance for high temperature heat pipe design.

2.2 INTRODUCTION

In the previous section, the frozen startup period of high-temperature heat pipes was successfully simulated by a comprehensive detailed numerical model. The model described the entire frozen startup process, and compared well with experimental data. While the numerical model is robust and is able to solve the problem in a general way, the time needed to develop the model and the computer resources needed to run the program make the model costly. Therefore, an analytical model is presented here, so that important system parameters can be related. While the applicability of such an analytical solution may be limited, it can aid in the understanding of the physical phenomena occurring in the problem.

Cotter (1967) developed an analytical model which incorporated the frontal startup behavior with a lumped one-dimensional effective thermal conductivity model. A major limitation of the above model was the need to know what the temperature of the heat pipe will be at a given power input, or what power will be transported at a given temperature before using the analytical results. For heat pipe operation, the relation between the working temperature and the power input is unknown a priori.

Sockol and Forman (1970) observed that at sufficiently high heat input levels, the evaporator wall temperature rose to some intermediate level during frozen startup of a lithium heat pipe, and remained almost constant as a steep temperature front moved down the length of the pipe. When the hot zone reached the condenser end cap, the heat pipe temperature increased to a steady-state value. Based on these observations, Sockol and Forman assumed the hot zone wall temperature was uniform, and the cold zone remained at the ambient temperature. Two lumped first-order differential equations for the wall temperatures were derived by making an energy balance over the evaporator and condenser sections. A one-dimensional vapor flow model was used, and it was assumed that the vapor velocity was sonic at the end of the hot zone. The temperature of the hot zone was obtained by solving the four coupled equations numerically. The numerical hot zone temperatures were compared with experimental data, and were 50 to 80°C higher than the measured values.

Since the uncertainty of the measured data was $\pm 30^{\circ}\text{C}$, the numerical solution was considered to be in good agreement.

Cao and Faghri (1992) derived a closed-form analytical solution based on the flat-front startup model. The results of the analytical solution are compared in the following section to experimental data and the numerical solutions given by Cao and Faghri (1993a) with good agreement.

2.3 ANALYTICAL SOLUTION

At sufficiently high heat input levels, the evaporator wall temperature of a liquid-metal heat pipe will rise to some intermediate level, and remain almost constant as a steep temperature front moves down the length of the pipe (Sockol and Forman, 1970; Faghri et al., 1991a; Ponnappan, 1989). The numerical solutions in the previous section showed that the vapor hot zone front was steeper than that of the wall temperature, and was located nearly in the middle of the slope region of the wall temperature distribution. Based on these facts, a flat-front frozen startup model is proposed to analyze the startup process of high-temperature heat pipes. At time t and $t + \delta t$, the actual heat pipe wall temperature distributions are shown schematically in Fig. 2.1 by two solid curves. The wall temperatures were approximated by the two dashed curves with linear profiles, where flat fronts are located in the middle of the slope regions of the wall temperature distributions. The temperatures of the

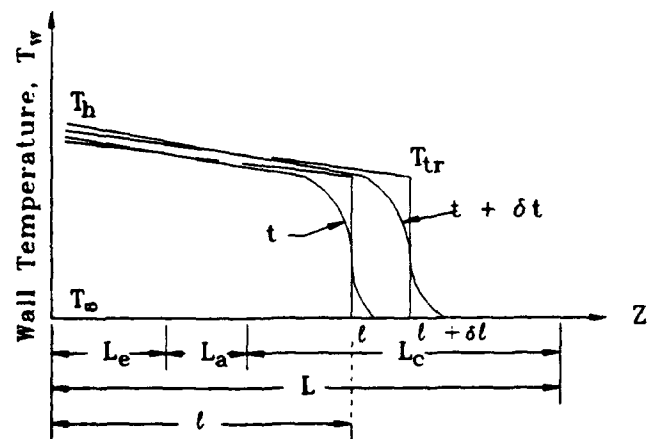


Figure 2.1: Description of the flat-front startup model

flat fronts were assumed to be at the continuum-rarefied transition temperature, T_{tr} . The hot zone wall temperature at the evaporator end cap is T_h . The hot zone lengths at time t and $t + \delta t$ are l and $l + \delta l$, respectively, where both T_h and l are functions of time.

The temperature of the evaporator section ($0 \leq z \leq L_e$) increases as heat is applied. Therefore, the hot zone length l should be equal to L_e before the temperature at the exit of the evaporator reaches the transition temperature T_{tr} and the hot zone begins to move into the adiabatic section. For $l = L_e$, a lumped energy balance results in an expression for the time needed for the evaporator exit temperature to reach the transition temperature when Q is constant.

$$t = CL_e(T_{aw} - T_\infty)/Q \quad (2.1)$$

where C is the heat capacity per unit length of the heat pipe, which includes the heat capacities of the wall and wick, and T_∞ is the initial (ambient) temperature of the heat pipe. The average hot zone wall temperature, T_{aw} , is based on a linear profile

$$T_{aw} = (T_h + T_{tr})/2 = \Delta T/2 + T_{tr} \quad (2.2)$$

where $\Delta T = T_h - T_{tr}$ is the total temperature drop across the hot zone.

An energy balance over the time interval t and $t + \delta t$ in terms of average hot zone temperature T_{aw} for the hot zone wall and wick gives

$$C \frac{d}{dt} [l(T_{aw} - T_{\infty})] + h^* [l(T_{aw} - T_{\infty})] = Q^* \quad (2.3)$$

where

$$h^* = 2\pi R_o h, \quad Q^* = Q + h^*(T_{aw} - T_{\infty})(L_e + L_a) \quad (2.4)$$

Q is the evaporator heat input, and h is the heat transfer coefficient at the condenser. The radial temperature difference in the wick and the wall, and the heat capacity of the vapor have been neglected in the above formulation. For noncircular heat pipes, $2\pi R_o$ should be replaced by the circumferential length W . In many cases, frozen startup is accompanied by a radiative boundary condition at the condenser. Therefore,

$$h^* = \frac{2\pi R_o q_c}{(T_{aw} - T_{\infty})} = 2\pi R_o \sigma \epsilon (T_{aw}^2 + T_{\infty}^2)(T_{aw} + T_{\infty}) \quad (2.5)$$

where q_c is the heat flux from the surface of the condenser. Equation (2.3) has a general solution assuming h^* is constant.

$$l(T_{aw} - T_{\infty}) = \exp\left(-\frac{h^* t}{C}\right) \int_{t_i}^t \left(\frac{Q^*}{C}\right) \exp\left(\frac{h^* t}{C}\right) dt + c_1 \exp\left(-\frac{h^* t}{C}\right) \quad (2.6)$$

where t_i is the initial time from which the solution is to be considered, and c_1 is a constant to be determined by the initial condition. In the adiabatic section, $L_e < l <$

$(L_e + L_a)$, the term h^* in eqn. (2.3) is zero.

$$l = Qt / [C(T_{aw} - T_\infty)] \quad (2.7)$$

Since eqns. 2.1 and 2.7 give the hot zone length as a function of time for the evaporator and adiabatic sections, eqn. (2.6) is used only for finding the solution for $l \geq (L_e + L_a)$. Therefore, the time when the hot zone reaches the condenser inlet is considered to be the initial time t_i for the solution of eqn. (2.6). The constant c_1 in eqn. (2.6) is

$$c_1 = (L_e + L_a)(T_{aw,i} - T_\infty) \exp\left(\frac{h^* t_i}{C}\right) \quad (2.8)$$

where $T_{aw,i}$ is the average hot zone wall temperature when the flat front reaches the condenser inlet. The time for the flat front to reach this point is

$$t_i = C(L_e + L_a)(T_{aw,i} - T_\infty)/Q \quad (2.9)$$

Therefore, eqn. (2.6) can be rewritten as

$$l = \frac{1}{(T_{aw} - T_\infty)} \exp\left(-\frac{h^* t}{C}\right) \int_{t_i}^t \left(\frac{Q^*}{C}\right) \exp\left(\frac{h^* t}{C}\right) dt + \frac{(L_e + L_a)(T_{aw,i} - T_\infty)}{(T_{aw} - T_\infty)} \exp\left[-\frac{h^*(t - t_i)}{C}\right] \quad (2.10)$$

It has been shown experimentally that the average hot zone temperature T_{aw} is a weak function of time for a constant Q . Therefore, Q^* can be assumed to be constant

in the integration, and eqn. (2.10) can be simplified to

$$l = \left[\frac{Q}{h^*(T_{aw} - T_\infty)} + (L_e + L_a) \right] \left[1 - \exp \left(-\frac{h^*(t - t_i)}{C} \right) \right] + \frac{(L_e + L_a)(T_{aw,i} - T_\infty)}{(T_{aw} - T_\infty)} \exp \left[\frac{-h^*(t - t_i)}{C} \right] \quad (2.11)$$

Equation 2.11 is applicable for $l \geq (L_e + L_a)$, and eqns. (2.1) and (2.7) should be used for $l = L_e$ and $L_e < l < (L_e + L_a)$, respectively. It can be seen that the above equations are functions of time t and average hot zone wall temperature T_{aw} . Therefore, the hot zone temperature distribution is found in the next section.

The heat pipe wall temperature is directly related to the vapor temperature distribution. By neglecting the radial heat conduction in the wick and wall, the temperature drop of the wall in the hot zone, ΔT , can be approximated to be the same as that of the vapor. It was shown that the total pressure drop for the laminar flow of vapor along the length of a heat pipe is

$$\Delta p = \frac{4\mu Q}{\pi \rho_v R_v^4 h_{fg}} (L_e + 2L_a + L_c) \quad (2.12)$$

For heat pipes without an adiabatic section, $L_a = 0$, eqn. (2.12) reduces to

$$\Delta p = \frac{4\mu Q}{\pi \rho_v R_v^4 h_{fg}} (L_e + L_c) = \frac{4\mu Q L_t}{\pi \rho_v R_v^4 h_{fg}} \quad (2.13)$$

where L_t is the total heat pipe length. In the flat-front startup model, the flat front

at the interface between the hot and cold zones is equivalent to the condenser end cap. Therefore, eqn. (2.13) is applied only to the vapor flow in the hot zone with l replacing L_t .

$$\Delta p = \frac{4\mu Ql}{\pi \rho_v R_v^4 h_{fg}} \quad (2.14)$$

The temperature drop ΔT corresponding to the pressure drop Δp is found by integrating the differential form of the Clausius-Clapeyron equation

$$\Delta T = \left(\frac{T}{\rho_v h_{fg}} \right)_{av} \Delta p \quad (2.15)$$

where $(T/\rho_v h_{fg})_{av}$ is the average value over the integration interval. The temperature drop can be found by combining eqns. (2.14) and (2.15).

$$\Delta T = \frac{4T_{av}\mu Ql}{\pi \rho_v^2 R_v^4 h_{fg}^2} \quad (2.16)$$

To account for vapor compressibility and density variation, the vapor density in eqn. (2.16) is assumed to be the average density corresponding to T_{av} . Combining the ideal gas law and the integrated form of the Clausius-Clapeyron equation gives

$$\rho_v = \frac{p_0}{R_g T_{av}} \exp \left[-\frac{h_{fg}}{R_g} \left(\frac{1}{T_{av}} - \frac{1}{T_0} \right) \right] \quad (2.17)$$

where p_0 and T_0 are the reference (saturation) pressure and temperature. By assuming a linear hot zone temperature and neglecting the radial temperature drop across the

wall and wick, we find that $T_{av} = T_{aw}$, where T_{aw} is given by eqn. (2.2). Combining eqns. (2.16), (2.17) and (2.2) gives

$$\frac{h_{fg}}{R_g} \left(\frac{1}{T_0} - \frac{1}{T_{tr} + \Delta T/2} \right) - \ln \left[\frac{R_g(T_{tr} + \Delta T/2)}{p_0} \left(\frac{4(T_{tr} + \Delta T/2)\mu Q l}{\pi \Delta T R_v^4 h_{fg}^2} \right)^{1/2} \right] = 0 \quad (2.18)$$

Equation 2.18 can be solved iteratively using the Newton-Raphson/secant method for the temperature drop, ΔT , and T_{aw} and T_h can be obtained from eqn. (2.2).

The analytical closed-form solutions for the hot zone length l as a function of time for the frozen startup period are obtained from eqn. (2.1) for $l = L_e$, eqn. (2.7) for $L_e < l < (L_e + L_a)$, and eqn. (2.11) for $(L_e + L_a) < l < L_t$. In all cases, eqn. (2.18) is used to find ΔT , and eqn. (2.2) is used to determine T_{aw} and T_h . The equations are solved sequentially as follows: For an initial hot zone length of l_i at an initial time t_i , the temperature drop over the hot zone is found from eqn. (2.18). The average hot zone wall temperature T_{aw} and the evaporator end cap temperature T_h are obtained from eqn. (2.2). Then, the hot zone length at time $t_i + \Delta t$, where Δt is the time step, can be calculated using eqn. (2.7) or eqn. (2.11), depending on the location of the hot zone front. The values of ΔT , T_{aw} , and T_h are calculated at time $t_i + \Delta t$ using the corresponding hot zone length obtained.

The closed-form analytical solution was compared to the experimental data for Case 13 of Faghri et al. (1991a, 1991b) in Fig. 2.2. The solution started from

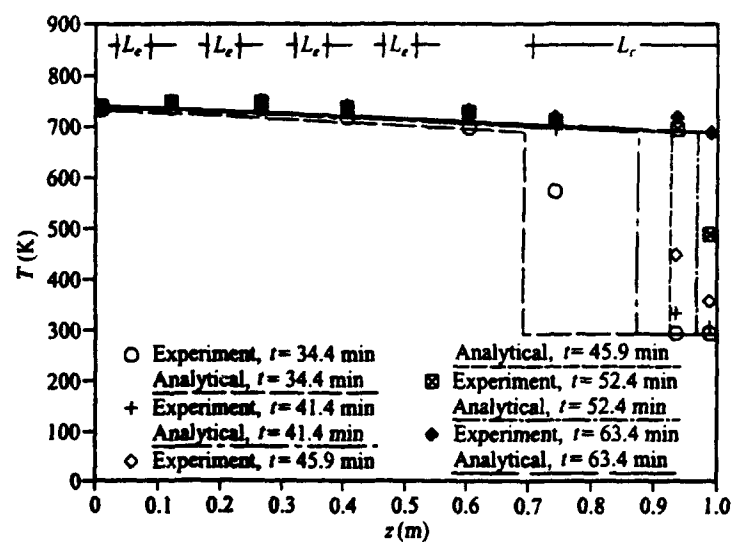


Figure 2.2: Analytical wall temperatures compared with experimental data for Case 13a

the inlet of the condenser, and eqn. (2.11) was used to calculate l from T_{aw} . The agreement between the analytical results and the experimental data is generally good. Figure 2.3 also compares the analysis with data from the case with $Q = 289.6$ W from Ponnappan (1989). The analytical results agree very well with the experimental data, except the curves nearest the condenser end caps. The data in that location indicated that vapor flow was still in the rarefied state. In eqn. (2.16), it can be seen that the temperature drop over the hot zone is dependent on the fourth power of the vapor space radius, R_v . For the heat pipe of Faghri et al. (1991a), $R_v = 10.75$ mm, and the temperature drop over the hot zone was relatively small. For the heat pipe by Ponnappan, $R_v = 6.35$ mm, and the temperature drop was significant. The analytical closed-form solution predicted the temperature drops over the hot zones for the two heat pipes remarkably well.

Figure 2.4 compares the numerical and analytical solutions of the outer wall temperature with the experimental data for Case 11a of Faghri et al. (1991a). The flat fronts of the analytical results intercept the numerical curves almost in the middle of the slope regions, and compare well with the numerical solution and the experimental data.

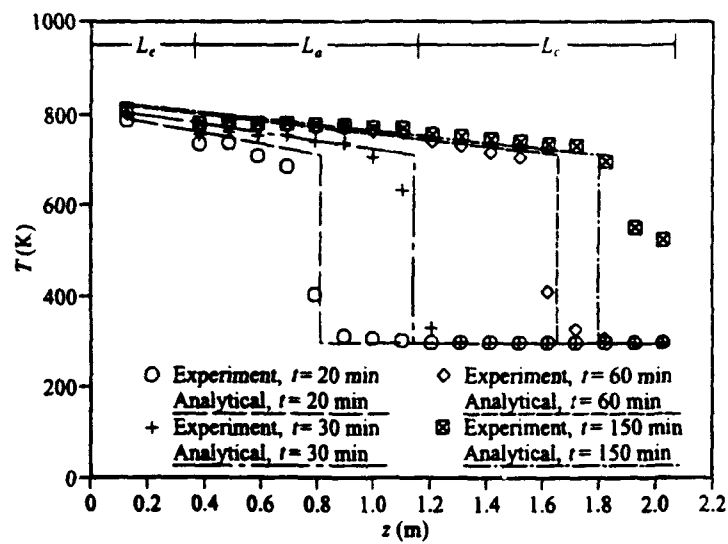


Figure 2.3: Analytical wall temperatures compared with experimental data given by Ponnappan (1989) for $Q = 289.6$ W

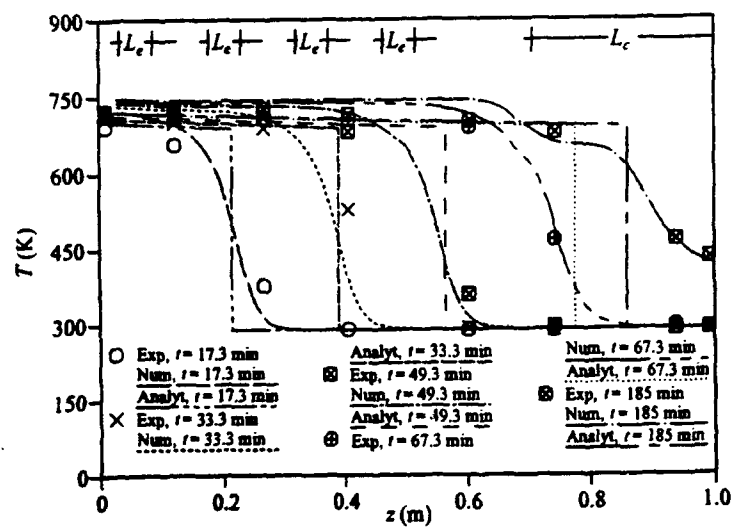


Figure 2.4: Analytical wall temperatures compared with experimental data and numerical solution for Case 11a

2.4 FROZEN-STARTUP LIMITATION

Heat pipe designs are generally based on the well-known performance limitations which are discussed extensively in Section 4. These are the sonic vapor velocity limit, the wick boiling limit, and the wick capillary limit. During the frozen startup process, the heat pipe may encounter the sonic limit, but this is a temporary condition which will disappear when the heat pipe working temperature rises to a sufficiently high level. The boiling limit rarely occurs in high-temperature heat pipes due to the high thermal conductivity of the liquid-metal working fluid and the thin wick structure. The capillary limit usually will not be encountered during the frozen startup process since the active length of the heat pipe is less than the total length. Therefore, with a proper design, the capillary limit should not occur. However, when heat is applied only in the evaporator region of a frozen heat pipe during startup, the working fluid may be frozen out of the evaporator to the adiabatic or condenser regions. In this case, a frozen-startup limit, which is different than the other limitations, needs to be considered (Cao and Faghri, 1992).

The frozen startup process is shown schematically in Fig. 2.5. The input heat flux q_e is applied at the evaporator and evaporation takes place at the wick-vapor interface. The vapor flows down the active length and condenses on the wick surface, releasing the latent heat of vaporization. A liquid-solid interface in the wick moves down the heat pipe with velocity W_i due to condensation onto the wick. The vapor

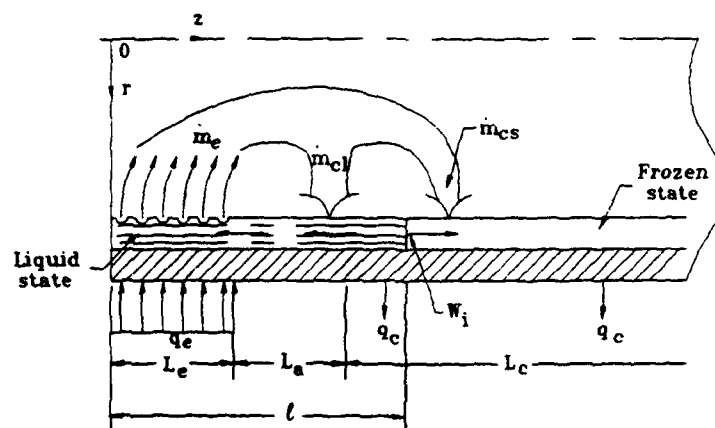


Figure 2.5: Description of the frozen-startup limit

leaves the evaporator section with mass flow rate \dot{m}_e . \dot{m}_{cl} is part of the total mass flow rate that condenses on the wick where the working fluid is melted. This part supplies liquid condensate to be pumped back to the evaporator by the capillary wick. The part of the mass flow rate of vapor which condenses on the solid-wick region, \dot{m}_{cs} , is frozen out and cannot flow back to the evaporator section. However, the movement of the liquid-solid interface in the wick down the length of the heat pipe will increase the mass of the liquid working fluid, which compensates for the mass loss due to the freezing out of vapor onto the frozen solid-wick surface. A mass balance of the liquid working fluid in the liquid-wick region requires

$$\varphi \rho_l A'_w W_i \geq \dot{m}_e - \dot{m}_{cl} = \dot{m}_{cs} \quad (2.19)$$

where φ is the porosity of the wick, ρ_l is the density of the liquid, and A'_w is the cross-sectional area of the wick saturated by the working fluid. Equation (2.19) indicates that the increase in the mass of liquid in the wick due to the liquid-solid interface movement must be greater than or equal to the mass loss due to the vapor freezing onto the solid-wick interface. If this condition is not met, liquid depletion in the evaporator occurs due to the vapor being frozen out. This relation was observed and defined as the frozen-startup limit (FSL) originally by Cao and Faghri (1992).

Frozen startup is characterized by the movement of the hot zone down the length of the heat pipe. At time t , as shown in Fig. 2.6, the location of the melting

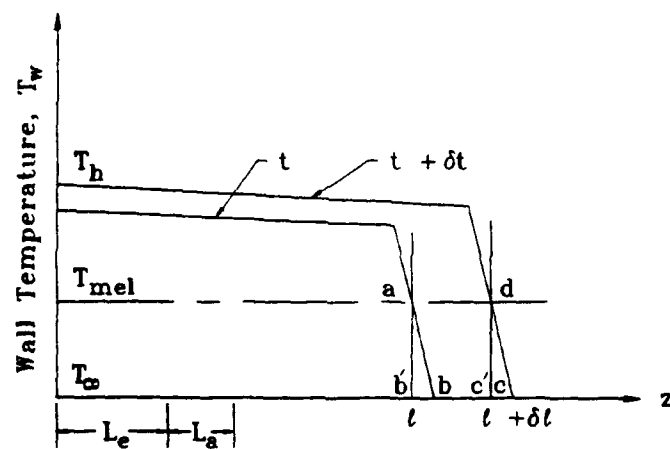


Figure 2.6: Description of the criterion for the frozen-startup limit

front is at $z = l$. At $t + \delta t$, the melting front moves to $l + \delta l$. The melting temperature T_{mel} intercepts the two temperature distributions at points a and d . The heat energy received by the part of the slope region whose temperature is below T_{mel} during the time interval δt is

$$Q_{cs}\delta t = C \cdot A_{a-b-c-d} \quad (2.20)$$

where C is the heat capacity per unit length and $A_{a-b-c-d}$ is the area enclosed by the curve connecting points a , b , c , and d . Since

$$A_{a-b-c-d} \simeq A_{a-b'-c'-d} = (T_{\text{mel}} - T_{\infty})\delta l \quad (2.21)$$

eqn. (2.20) can be approximated to be

$$Q_{cs}\delta t = C(T_{\text{mel}} - T_{\infty})\delta l \quad (2.22)$$

The corresponding mass of vapor that condensed onto the frozen wick during δt , neglecting axial conduction, is

$$\delta m_{cs} = \dot{m}_{cs}\delta t = Q_{cs}\delta t/h_{fg} = C(T_{\text{mel}} - T_{\infty})\delta l/h_{fg} \quad (2.23)$$

The mass condensation rate is

$$\dot{m}_{cs} = \delta m_{cs} / \delta t = \frac{C(T_{\text{mel}} - T_{\infty})}{h_{fg}} \frac{\delta l}{\delta t} \quad (2.24)$$

The rate of increase of the liquid mass is $\varphi \rho_{\ell} A'_w W_i$, where the time rate of change of the hot zone length is

$$\frac{\delta l}{\delta t} = W_i \quad (2.25)$$

Substituting eqns. (2.24) and (2.25) into equ. (2.19) and rearranging gives

$$\text{FSL} = \frac{\varphi \rho_{\ell} A'_w h_{fg}}{C(T_{\text{mel}} - T_{\infty})} \geq 1 \quad (2.26)$$

Equation (2.26) is an approximate expression of the frozen-startup limit for high-temperature heat pipes. For a circular cross-section heat pipe,

$$A'_w = 2\pi R_v \delta'_\ell \quad (2.27)$$

where R_v is the vapor space radius and δ'_ℓ is the thickness of the working fluid in the wick structure. It should be pointed out that for normal operation, δ'_ℓ may not be equal to the wick structure thickness δ_ℓ . Also, for a circular heat pipe,

$$C(T_{\text{mel}} - T_{\infty}) \simeq (2\pi R_v \delta'_\ell c_{me} \rho_{\text{eff}} + 2\pi R_o \delta_w c_w \rho_w)(T_{\text{mel}} - T_{\infty}) + 2\pi R_v \delta'_\ell H \rho_{\ell} \varphi \quad (2.28)$$

where c_{me} is the average effective specific heat of the wick over the liquid-wick and

solid-wick, ρ_{eff} is the effective density of the wick, δ_w is the wall thickness, and H is the latent heat due to melting. Equation (2.26) can be rewritten as

$$\text{FSL} = \frac{\varphi \rho_\ell R_v \delta'_\ell h_{fg}}{(R_v \delta'_\ell c_{me} \rho_{\text{eff}} + R_o \delta_w c_w \rho_w)(T_{\text{mel}} - T_\infty) + R_v \delta'_\ell H \rho_\ell \varphi} \geq 1 \quad (2.29)$$

For a thick wall or wick, R_o and R_v in eqn. (2.29) should be replaced by the average radius of the wall, $R_{wo} = (R_w + R_o)/2$, or the average radius of the wick, $R_{vw} = (R_v + R_w)/2$.

The frozen-startup limit was applied to the heat pipe studied by Faghri et al. (1991a), which resulted in

$$\text{FSL} \simeq 1.46 > 1$$

This indicates that the heat pipe should not have encountered the frozen-startup limit, which was indeed the case. It should be noted that FSL was very close to unity for the heat pipe studied by Faghri et al., which means that the frozen-startup limit does need to be considered in the design process. The calculation was also made for the heat pipe described by Ponnappan (1989), with the following result.

$$\text{FSL} \simeq 1.82 > 1$$

Again, no problems were encountered by Ponnappan during the startup process. From eqns. (2.26) and (2.29), it can be seen that a larger working fluid inventory and larger

evaporation latent heat aid in frozen startup, while a larger heat capacity and higher melting temperature have an opposite effect. The frozen-startup limit provides a tool which will aid designers in avoiding difficulties during the frozen startup period.

TRANSIENT TWO-DIMENSIONAL GAS-LOADED HEAT PIPE ANALYSIS

3.1 SUMMARY

A two-dimensional, transient mathematical model that accounts for diffusion and variable properties on the operation of a heat pipe is presented. The major advantage over previous models is that this model treats the noncondensable gas as a separate

entity which is described by mass transport phenomena. Also, the energy transport through the wall is coupled to the transient operation of the heat pipe through the use of a conjugate solution technique. The complete behavior of the heat pipe, along with the location and two-dimensional shape of the noncondensable gas front, are modeled from the initial continuum flow, liquid state startup to steady-state conditions. The proposed model predicted the existing experimental data for the operation of high-temperature heat pipes with and without noncondensable gases.

3.2 INTRODUCTION

Gas-loaded heat pipes have been applied in many diverse fields, and are useful when the temperature of a device must be held constant while a variable heat load is dissipated. However, their use is limited by the lack of a complete understanding of the performance of these devices, particularly during transient operation.

Gas-loaded heat pipes have been previously modeled with several levels of approximation. The classical flat-front analytical model of Marcus and Fleishman (1970) neglected all diffusion across the vapor-gas interface. Later studies modeled one-dimensional steady diffusion (Edwards and Marcus, 1972), and one-dimensional transient diffusion (Shukla, 1981). Rohani and Tien (1973) studied the steady-state two-dimensional diffusion process in a gas-loaded heat pipe. The importance of modeling radial diffusion in a gas-loaded heat pipe was demonstrated where the noncon-

densible gas tends to accumulate at the liquid-vapor interface, which retards vapor condensation. However, Rohani and Tien (1973) neglected the effect of conjugate heat transfer through the wall as well as transient effects. The transient response of a gas-loaded heat pipe was shown to be important by Shukla (1981) as transient thermal overshoots were discovered. However, this study did not include the effects of radial heat conduction in the wall or wick, nor the radial diffusion effects of the noncondensable gas.

Cao and Faghri (1990) presented a two-dimensional transient analysis of heat pipe dynamics. The analysis included the compressible vapor flow and the coupling between the heat pipe wall/wick and the vapor flow. However, the analysis was limited to the conventional heat pipe without noncondensable gas.

In the present study, the two-dimensional, transient gas-loaded heat pipe operation, including the effects of conjugate heat transfer through the wall, is modeled through a solution of the general differential conservation equations. This procedure was used to simulate the high temperature heat pipe experimentally studied by Ponnappan (1989) both with and without noncondensable gases.

3.3 MATHEMATICAL MODELING

3.3.1 Vapor Space

The physical configuration and coordinate system of the gas-loaded heat pipe studied is shown in Fig. 3.1. Gas-loaded heat pipes offer isothermal operation for varying heat loads by changing the overall thermal resistance of the heat pipe. As the heat load increases, the vapor temperature and total pressure increase in the heat pipe. This increase in total pressure compresses the noncondensable gas in the condenser, increasing the surface area available for heat transfer, which maintains a nearly constant heat flux and temperature.

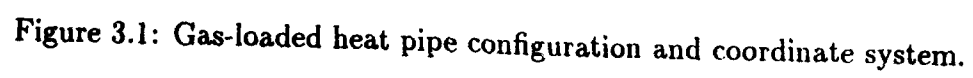
The differential conservation equations for transient, compressible, two-species flow with constant viscosity are as follows (Ganic et al., 1985; Bird et al., 1960)

Mass:

$$\frac{\partial \bar{\rho}}{\partial t} + \frac{1}{r} \frac{\partial}{\partial r}(\bar{\rho} r v) + \frac{\partial}{\partial z}(\bar{\rho} w) = 0 \quad (3.1)$$

Momentum:

$$\bar{\rho} \frac{D\vec{V}}{Dt} = -\nabla \bar{p} + \frac{1}{3} \bar{\mu} \nabla (\nabla \cdot \vec{V}) + \bar{\mu} \nabla^2 \vec{V} \quad (3.2)$$



Energy:

$$\frac{DT}{\bar{\rho} \bar{c}_p} - \nabla \cdot \bar{k} \nabla T - \nabla \cdot \left(\sum_{j=1}^2 D_{d,j} c_{p,j} T \nabla \rho_j \right) - \frac{D\bar{p}}{Dt} - \bar{\mu} \Phi = 0 \quad (3.3)$$

where subscript j denotes either vapor or gas.

Species:

$$\frac{D\rho_g}{Dt} - \nabla \cdot D_{gv} \nabla \rho_g = 0 \quad (3.4)$$

where

$$\Phi = 2 \left[\left(\frac{\partial v}{\partial r} \right)^2 + \left(\frac{v}{r} \right)^2 + \left(\frac{\partial w}{\partial z} \right)^2 \right] + \left(\frac{\partial v}{\partial z} + \frac{\partial w}{\partial r} \right)^2 - \frac{2}{3} \left[\frac{1}{r} \frac{\partial}{\partial r} (rv) + \frac{\partial w}{\partial z} \right]^2 \quad (3.5)$$

where v and w are the radial and axial vapor velocities, \bar{p} is the total mixture pressure, $\bar{\mu}$ is the mass-fraction-weighted mixture viscosity, \bar{c}_p is the specific heat of the mixture, \bar{k} is the thermal conductivity of the mixture, D_d is the self-diffusion coefficient for both the vapor and gas species, D_{gv} is the mass diffusion coefficient of the vapor-gas pair, ρ_g is the density of the noncondensable gas, and the mixture density is $\bar{\rho} = \rho_g + \rho_v$. The partial gas density is determined from the species equation and the vapor density is found from the ideal gas relation using the partial vapor pressure.

The two choices in species conservation formulation are mass and molar fraction. Molar fraction offers the possibility of a direct simplification in the formulation by the assumption of constant molar density. This assumption is valid over a

wider range of temperature and pressure than the corresponding assumption of constant mass density. However, when molar fractions are used, the momentum equation must be written in terms of molar-weighted velocities. The resulting equation cannot be written in terms of the total material derivative, and is significantly more difficult to solve.

A benefit of the general equation formulation is the allowance for variable properties. Typical of compressible gas applications, the density is related to the temperature and pressure through the equation of state

$$\bar{p} = \frac{\bar{\rho} \mathbf{R} T}{\bar{M}} \quad (3.6)$$

where \bar{M} is the molecular weight of the vapor-gas mixture, and \mathbf{R} is the universal gas constant.

In the species equation, D_{gv} is a function of pressure and temperature. For a vapor-gas mixture of sodium-argon, the relationship for D_{gv} is (Edwards et al., 1979)

$$D_{gv} = 1.3265 \times 10^{-3} T^{3/2} (\bar{p})^{-1} \quad (3.7)$$

where T is in Kelvin, \bar{p} is in N/m^2 , and D_{gv} is in m^2/s . Following a similar procedure, the variable diffusion coefficient formulation for the sodium-helium pair is (Edwards et al., 1979)

$$D_{gv} = 1.2795 \times 10^{-3} T^{3/2} (\bar{p})^{-1} \quad (3.8)$$

The interspecies heat transfer which occurs through the vapor-gas mass diffusion was modeled with a self-diffusion model, as described by Bird et al. (1960). In the present model, however, the self-diffusion coefficient, D_d , was assumed constant at the initial temperature of the heat pipe.

3.3.2 Wall and Wick

In the heat pipe wall, heat transfer is described by the transient two-dimensional conduction equation

$$\rho_w c_{pw} \frac{\partial T}{\partial t} = k_w \left[\frac{1}{r} \frac{\partial}{\partial r} \left(r \frac{\partial T}{\partial r} \right) + \frac{\partial^2 T}{\partial z^2} \right] \quad (3.9)$$

where the subscript w denotes the heat pipe wall material. In the heat pipe wick, the model uses the conduction simplification discussed by Cao and Faghri (1990). This assumption states that, for thin wicks and working fluids with high thermal conductivities, the effect of convection due to the liquid flow in the porous wick is

negligible. Therefore, heat transfer in the wick is by conduction only, as described by:

$$(\rho c_p)_{\text{eff}} \frac{\partial T}{\partial t} = k_{\text{eff}} \left[\frac{1}{r} \frac{\partial}{\partial r} \left(r \frac{\partial T}{\partial r} \right) + \frac{\partial^2 T}{\partial z^2} \right] \quad (3.10)$$

where $(\rho c_p)_{\text{eff}} = \varphi(\rho c_p)_\ell + (1 - \varphi)(\rho c_p)_s$, φ is the wick porosity and $(\rho c_p)_s$ is the heat capacity of the solid wick structure. k_{eff} is the effective thermal conductivity of the wrapped screen wick structure (Chi, 1976):

$$k_{\text{eff}} = \frac{k_\ell[(k_\ell + k_s) - (1 - \varphi)(k_\ell - k_s)]}{[(k_\ell + k_s) + (1 - \varphi)(k_\ell - k_s)]} \quad (3.11)$$

3.3.3 Boundary Conditions

At the end caps of the heat pipe, the no-slip condition for velocity, the adiabatic condition for temperature, and the overall gas conservation conditions are imposed.

$$\text{At } z = 0: \quad v = w = \frac{\partial T}{\partial z} = \frac{\partial \rho_g}{\partial z} = 0 \quad (3.12)$$

$$\text{At } z = L: \quad v = w = \frac{\partial T}{\partial z} = 0, \quad \rho_g = \rho_{g,BC} \quad (3.13)$$

where $\rho_{g,BC}$ is iteratively adjusted to satisfy overall conservation of noncondensable gas. This boundary condition is implemented through the calculation of the total

mass of noncondensable gas in the heat pipe. If the total mass is found to be less than the mass initially present in the pipe, the boundary value is increased by 10% of the previous value. Conversely, if the calculated mass is larger than that initially present, the boundary value is decreased. This ensures the conservation of the overall mass to within a preset tolerance, which is 1% in the present formulation. The symmetry of the cylindrical heat pipe requires that the radial vapor velocity and the gradients of the axial vapor velocity, temperature, and gas density are zero at the centerline ($r = 0$):

$$v = \frac{\partial w}{\partial r} = \frac{\partial T}{\partial r} = \frac{\partial \rho_g}{\partial r} = 0 \quad (3.14)$$

The liquid-vapor interface ($r = R_v$) is impermeable to the noncondensable gas.

$$\dot{m}_g = S_\delta A D_{gv} \nabla \rho_g + \rho_g S_\delta \vec{V} = 0 \quad (3.15)$$

where S_δ is the surface area of the heat pipe core. This formulation of \dot{m}_g accounts for both convective and diffusive noncondensable gas mass fluxes at the vapor-liquid interface. To ensure saturation conditions in the evaporator section (and part of the adiabatic section since the exact transition point is determined iteratively), the Clausius-Clapeyron equation is used to determine the interface temperature as a function of pressure. The interface radial velocity is then found through the evaporation rate required to satisfy heat transfer requirements. The no-slip condition is still in effect for the axial velocity component.

At $r = R_v$ for $z \leq L_e + L_a$:

$$T_{\text{sat}} = \left(\frac{1}{T_0} - \frac{R}{M_v h_{fg}} \ln \frac{p_v}{p_0} \right)^{-1} \quad (3.16)$$

$$v_\delta = \frac{\left(k_{\text{eff}} \frac{\partial T_\ell}{\partial r} - \bar{k}_\delta \frac{\partial T_v}{\partial r} \right)}{\left(h_{fg} + \bar{c}_{p\delta} T_{\text{sat}} \right) \bar{\rho}_\delta} \quad (3.17)$$

$$w = 0 \quad (3.18)$$

where \bar{k}_δ , $\bar{c}_{p\delta}$ and $\bar{\rho}_\delta$ are the vapor-gas mixture properties at the liquid-vapor interface. In eqn. (16), the saturation temperature of the vapor is found from the partial vapor pressure. A solution of the momentum equation gives the total mixture pressure, but the partial vapor pressure can be found from using the local gas density.

$$p_v = \frac{\bar{M}}{M_v} \bar{p} \left(1 - \frac{\rho_g}{\bar{\rho}} \right) \quad (3.19)$$

This equation was derived assuming a mixture of ideal gases following Dalton's model for mixtures.

At the liquid-vapor interface in the active portions of the condenser section, vapor condenses and releases its latent heat energy. This process is simulated by applying a heat source at the interface grids in the condenser section. The interface velocity can be obtained through a mass balance between the evaporator and condenser section allowing for inactive sections of condenser.

At $r = R_v$ for $z > L_e + L_a$:

$$q_{so} = - (h_{fg} + \bar{c}_{p\delta} T_\delta) (\bar{\rho} - \rho_g) v_\delta \quad (3.20)$$

Due to the conjugate nature of the solution procedure, the boundary condition between the wick and the wall is automatically satisfied. This condition requires the equality of the heat fluxes into and out of the wick-wall interface ($r = R_w$).

$$k_w \frac{\partial T}{\partial r} = k_{\text{eff}} \frac{\partial T}{\partial r} \quad (3.21)$$

At the outer pipe wall surface, the boundary conditions depend on both the axial position and the mechanism of heat transfer being studied. In the evaporator, a constant heat flux is specified. In the condenser, a radiative boundary condition is imposed.

Evaporator:

$$k_w \frac{\partial T}{\partial r} \Big|_{r=R_o} = q_e \quad (3.22)$$

Adiabatic:

$$\frac{\partial T}{\partial r} \Big|_{r=R_o} = 0 \quad (3.23)$$

Condenser:

$$-k_w \frac{\partial T}{\partial r} \Big|_{r=R_o} = \sigma \epsilon (T_w^4 - T_\infty^4) \quad (3.24)$$

3.3.4 Initial Conditions

Since this model simulates the transient operation of a gas-loaded heat pipe, the initial physical conditions of the heat pipe are required for a solution of the problem. The initial temperature is uniform throughout the heat pipe at the start of the simulation. There is no motion of either the gas or vapor, and the noncondensable gas is evenly distributed throughout the vapor space by diffusion. The initial temperature of the heat pipe is above the free-molecular/continuum-flow transition temperature for the specific heat pipe vapor diameter (Cao and Faghri, 1993).

3.4 NUMERICAL METHODOLOGY

The numerical procedure used in this model is the SIMPLE method (Patankar, 1980). Discretizing the differential equations resulted in a system of algebraic equations in terms of T , w , v , and ρ_g . This system of equations was solved using the Thomas or tri-diagonal matrix algorithm.

The numerical procedure is as follows:

1. Input the initial conditions.
2. Initialize the pressure, temperature, gas density, and velocity fields.
3. Solve the momentum equations using the mixture density to obtain v^* and w^* , which are the vapor velocities based on the guessed pressure.

4. Solve for the new pressure field and update the previous pressure field.
5. Calculate v and w from their starred values using velocity correction formulas.
6. Solve the energy equation.
7. Solve the mass transport equation.
8. Using the mixture molecular weight, determine the new \bar{p} from the equation of state.
9. Steps 3-8 are repeated until convergence is reached.

There are two possible methods to account for vapor compressibility. The first method is to use a density correction formulation

$$\rho = \rho^* + \rho' = \rho^* + K_p p' \quad (3.25)$$

where $K_p = \partial \rho / \partial p$, and p' is the guessed pressure. The second method uses the ideal gas relationship in conjunction with an additional term in the energy equation. In this method, the pressure is chosen as the dependent variable and the vapor density is determined directly. The additional term in the energy equation accounts for the temperature variation caused by the high vapor velocities, and must be included when using the equation of state. In the present analysis, the ideal gas relationship resulted in better convergence characteristics. When the vapor flow was subsonic, it was found

that both methods gave very similar results.

In the present study, a uniform axial grid and a nonuniform radial grid were used. The numerical simulation used 12 (radial) \times 55 (axial) cells for the 2.0 m long heat pipe. The numerical model was run for several different grid distributions with less than a 3% maximum deviation between the solutions. The number of cells used were chosen to optimize the accuracy of the solution versus the required computer time. The physical properties at the interface are based on the harmonic average of the properties at the adjacent cells (Patankar, 1980).

3.5 RESULTS AND DISCUSSION

Validation of the present numerical heat pipe model was accomplished by simulating four cases of experimental data by Ponnappan (1989), which are shown in Table 3.1. The heat pipe geometry and operating conditions are shown in Table 3.2. Vector and contour plots for Case 1 are shown in Fig. 3.2, where the effect of vapor compressibility can be seen. Due to the small vapor space and high heat input, the vapor velocity is very high (~ 330 m/s). For sodium, this velocity corresponds to a Mach number of approximately 0.5. From Fig. 3.2(a), a temperature decrease can be seen at the exit of the evaporator section, where the maximum velocity occurs. Furthermore, as the vapor velocity decreases, a temperature recovery can be seen in the condenser section. Also shown in Fig 3.2(a) are the temperature drop across the wall and wick.

Table 3.1: Operating conditions for various cases

Case Number	Gas Pressure (torr)	Mass of Gas (kg)	Heat Load (W)	Condenser Emissivity
1	0.0	0.0	515	0.3
2	1.35	3.66×10^{-7}	451	0.56
3	1.35	3.66×10^{-7}	258 to 306	0.3
4	1.35	3.66×10^{-7}	258 to 451	0.3

Table 3.2: Heat pipe geometry and parameters

Parameter	
Wall	304 SS
Wick	wire mesh
Working Fluid	Sodium
Buffer Gas	Argon
L_t	2.03 m
L_e	0.375 m
L_a	0.745 m
L_c	0.91 m
R_v	0.00635 m
R_o	0.0111 m
δ_w	0.00165 m
k_{eff}	39 W/m · K
k_ℓ	70.08 W/m · K
k_w	20 W/m · K
μ_v	1.8×10^{-5} kg/m · s
ρ_v	0.003 kg/m ³
ρ_ℓ	828.1 kg/m ³
$c_{p,v}$	904 J/kg · K
h_{fg}	4.37×10^6 J/kg
φ	0.66
T_∞	300 K

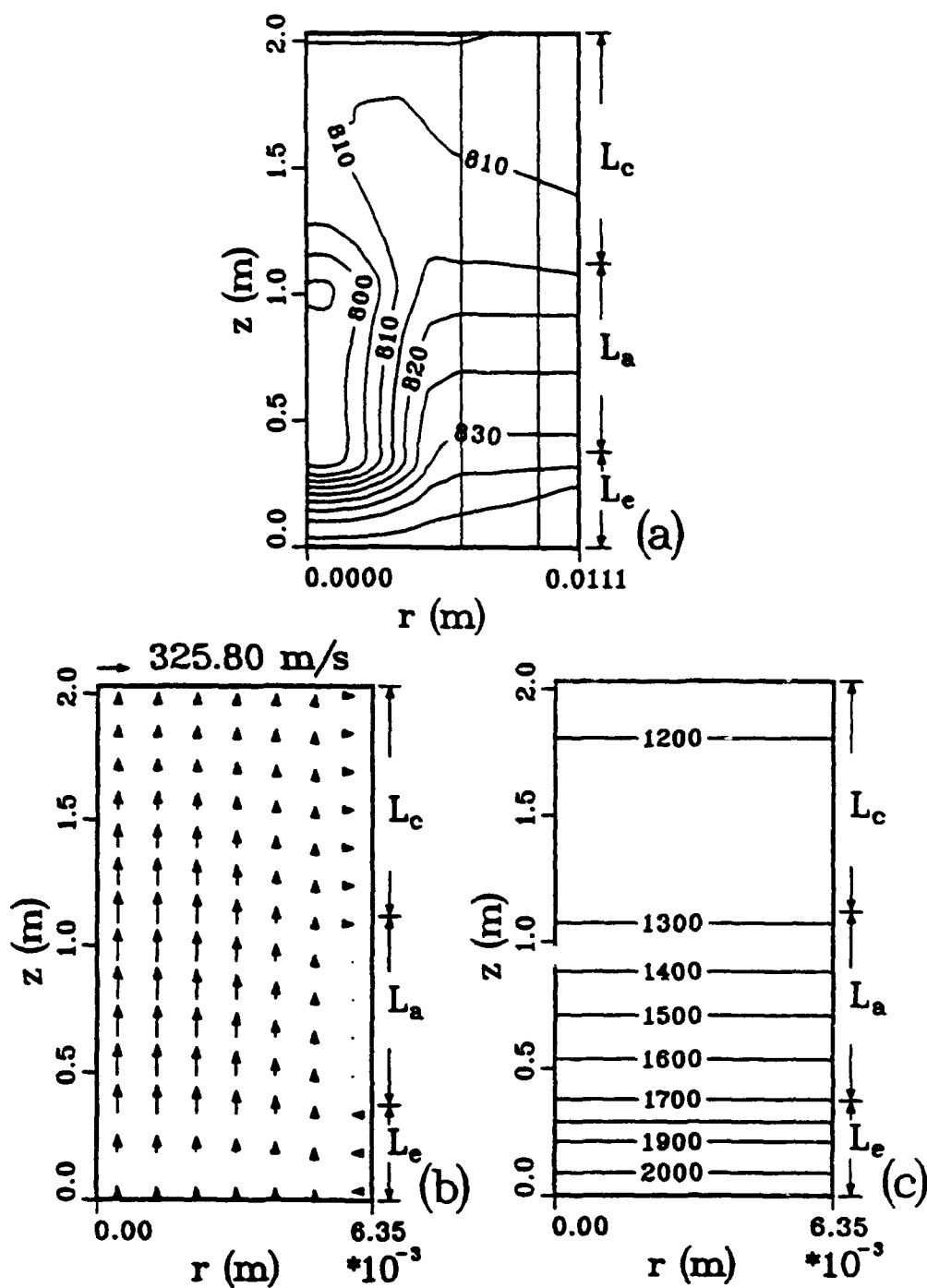


Figure 3.2: Numerical simulation of the high-temperature heat pipe (Case 1): (a) Vapor temperature contours; (b) Vapor velocity vectors in the r - z plane; (c) Vapor pressure contours.

The temperature profiles in the wall are nearly linear since the thermal conductivity of the stainless-steel pipe wall is relatively low. However, the direction of the temperature gradients in the respective sections can be seen. As expected, the temperature gradient is positive in the evaporator as heat is being added to the pipe. Likewise, the temperature gradient is zero in the adiabatic section and negative in the condenser section.

The vapor velocity vectors in the r - z plane are shown in Fig. 3.2(b). Since the evaporator section is much shorter than the condenser section, the radial vapor velocity in the evaporator is much higher than that in the condenser. The highest vapor velocity occurs at the centerline of the heat pipe, as expected.

The vapor pressure contours are shown in Fig. 3.2(c), where the two-dimensional effects are seen to be negligible. This was expected since the vapor space diameter for this heat pipe is very small. More importantly, the vapor temperature and pressure are not dependent in the vapor space. In a heat pipe, phase change occurs only at the vapor-liquid interface, which implies that saturation conditions are seen only at the interface. In the vapor space, however, the saturation relation does not necessarily apply, where the vapor temperatures are determined from energy requirements, accounting for viscous and compressible effects. The transient axial temperature profiles for the no-gas case are shown in Fig. 3.3 for Case 1. From Fig. 3.3(a), the comparison with the experimental data is very good. The transient

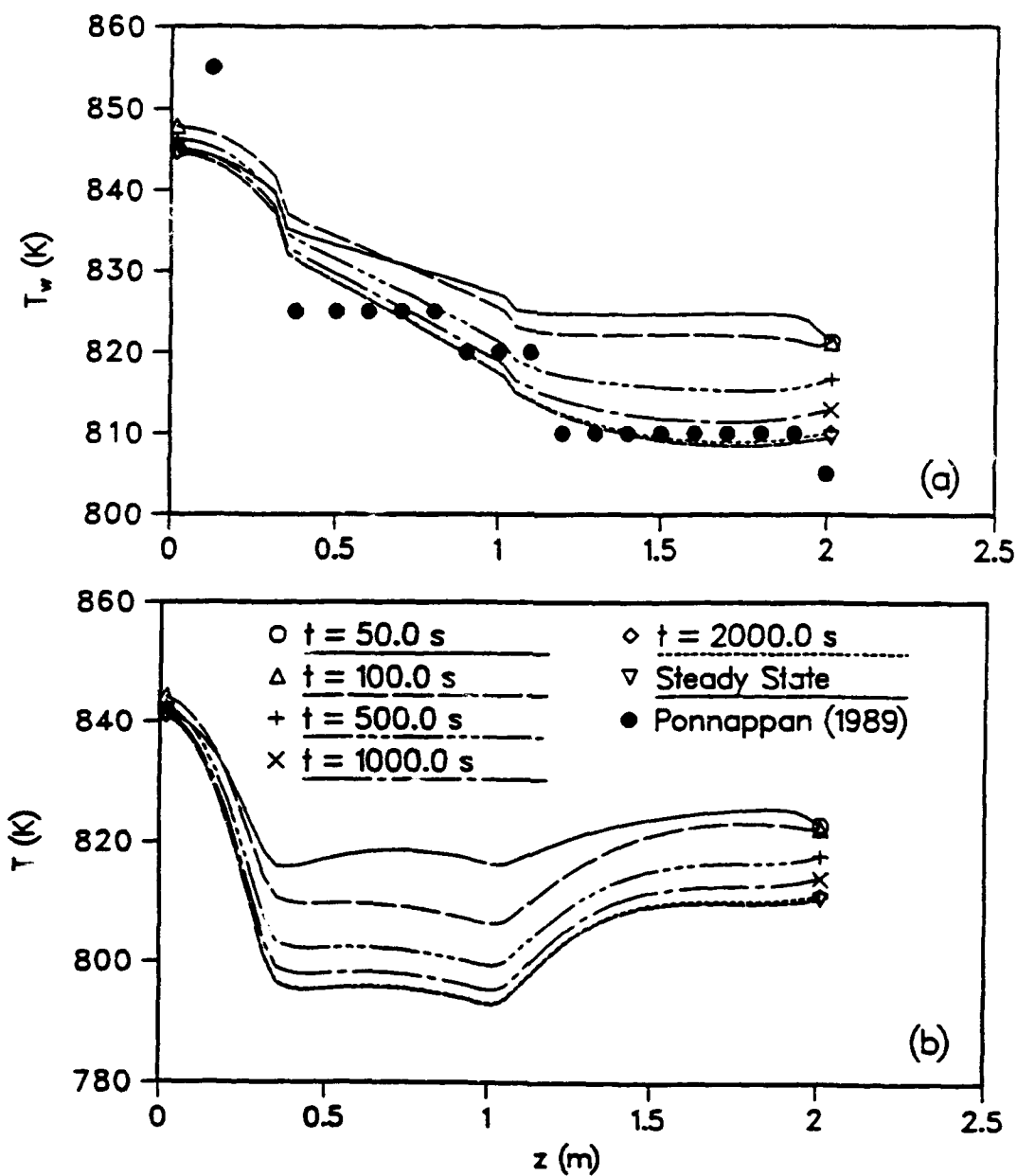


Figure 3.3: Temperature profiles for conventional heat pipe with $Q_{in} = 515$ W (Case 1): (a) Transient wall temperature profile; (b) Transient centerline temperature profile.

time for this heat pipe is approximately 2000 s. The vapor dynamics for this case are shown in Fig. 3.4.

The gas-loaded heat pipe experimentally studied by Ponnappan was simulated (Case 2), with results shown in Figs. 3.5 and 3.6. This case has a higher radiative emissivity than Case 1, which results in a decrease in the thermal resistance at the outer condenser surface. In the experiment performed by Ponnappan, the emissivity was increased when the noncondensable gas was added, so that a near-constant operating temperature (compared to Case 1) could be maintained. In Fig. 3.5, the wall and vapor temperatures decreased significantly in the condenser section due to the presence of the noncondensable gas. The gas density increased in the condenser during the transient operation, as shown in Fig. 3.6(a). The steady state wall temperature is in good agreement with the data by Ponnappan.

To further validate the numerical procedure, the gas-loaded heat pipe of Ponnappan with a low radiative emissivity (Case 3) was simulated. The velocity vector and contour plots for the gas-loaded case with a low radiative emissivity (Case 3) are shown in Fig. 3.7. In Fig. 3.7(a), the temperature distribution for the gas-loaded case is significantly different from that of the no-gas case. As expected, there is a large temperature drop across the inactive condenser section, and the radial temperature variations in this section are relatively uniform. This is due to the low vapor velocities in this region and the resulting low convective heat transfer in the

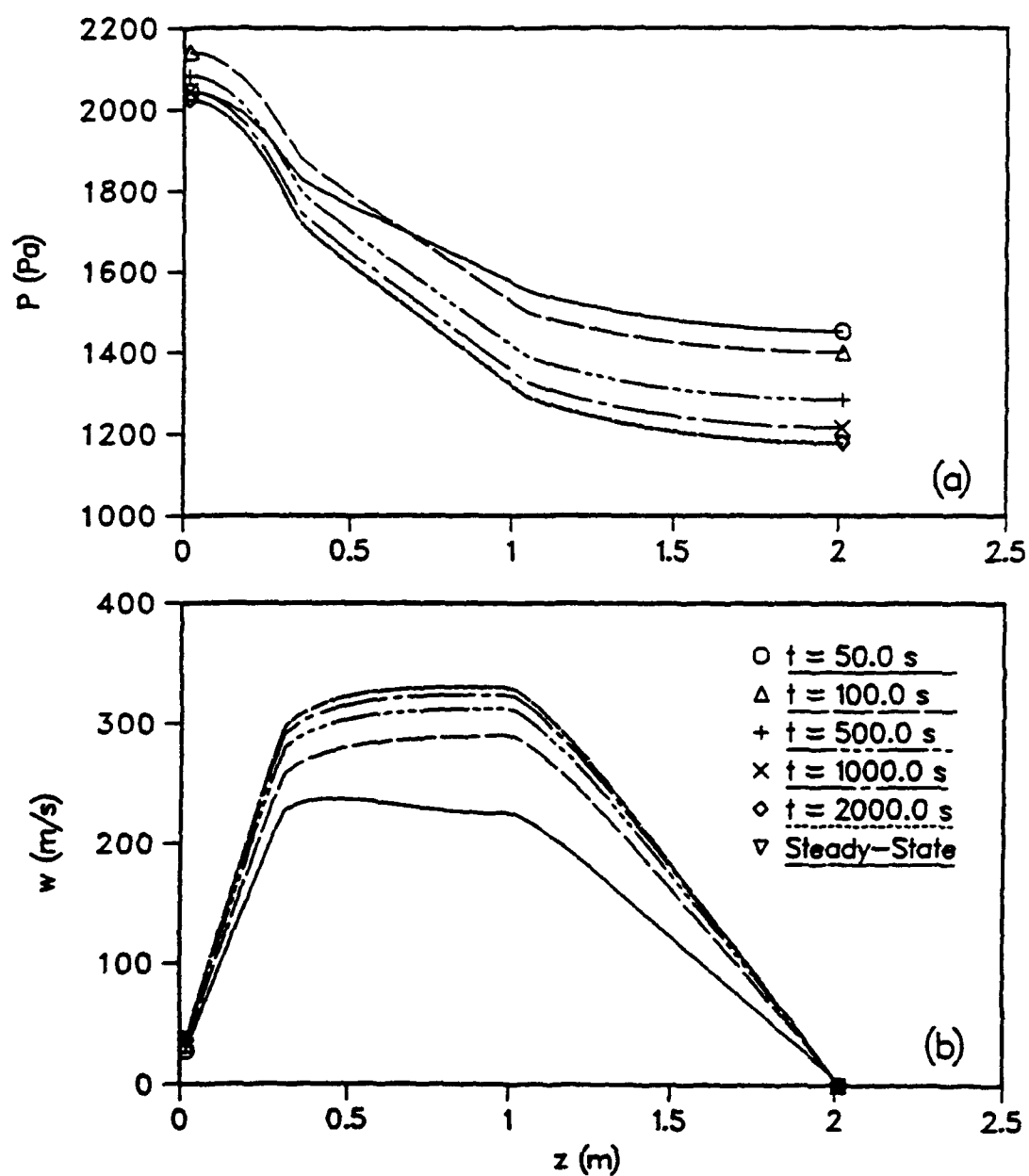


Figure 3.4: Vapor flow dynamics for conventional heat pipe with $Q_{in} = 515$ W (Case 1): (a) Transient centerline pressure profile; (b) Transient centerline axial velocity profile.

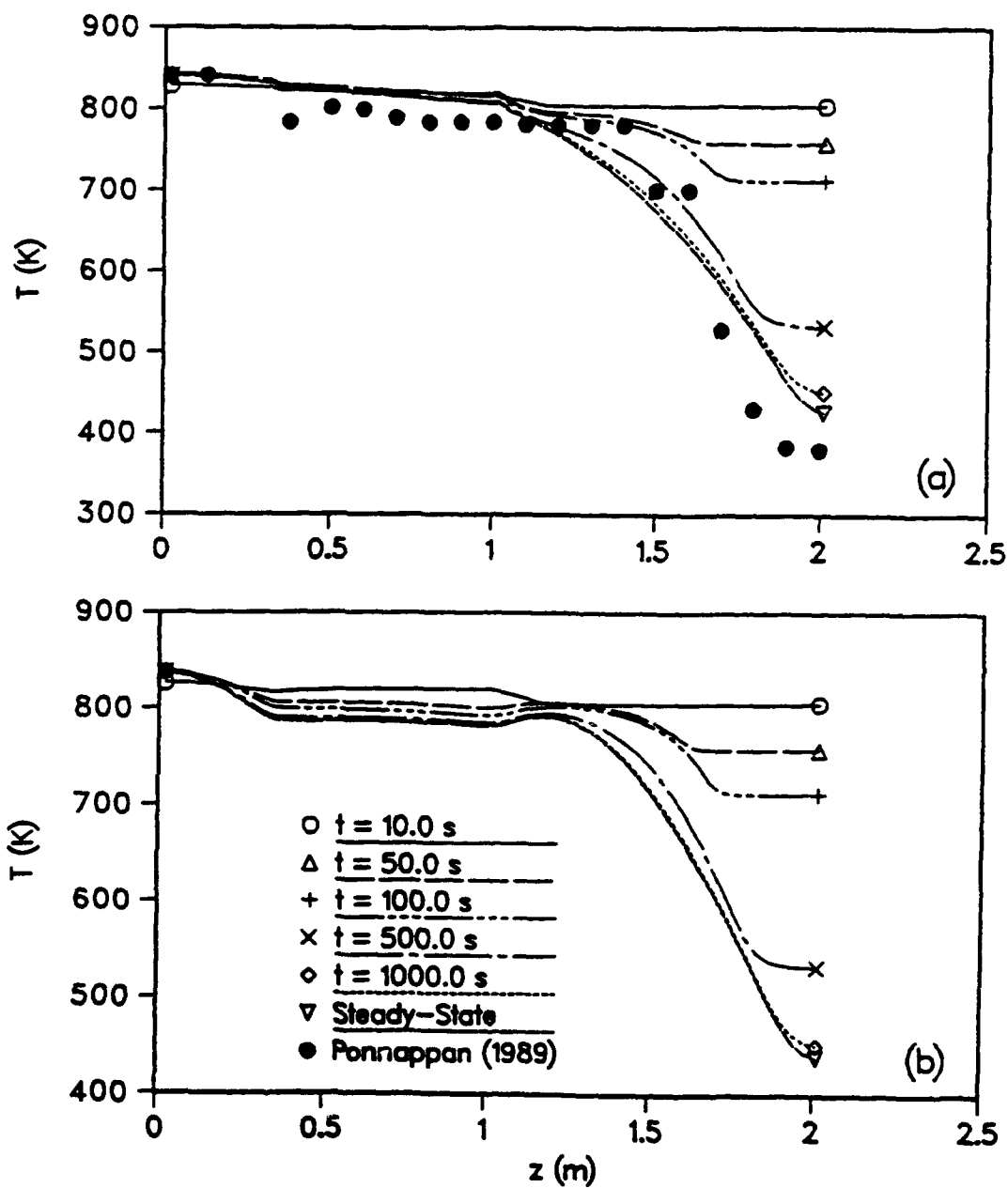


Figure 3.5: Temperature profiles for gas-loaded heat pipe with $Q_{in} = 451$ W (Case 2):

(a) Transient wall temperature profile; (b) Transient centerline temperature profile.

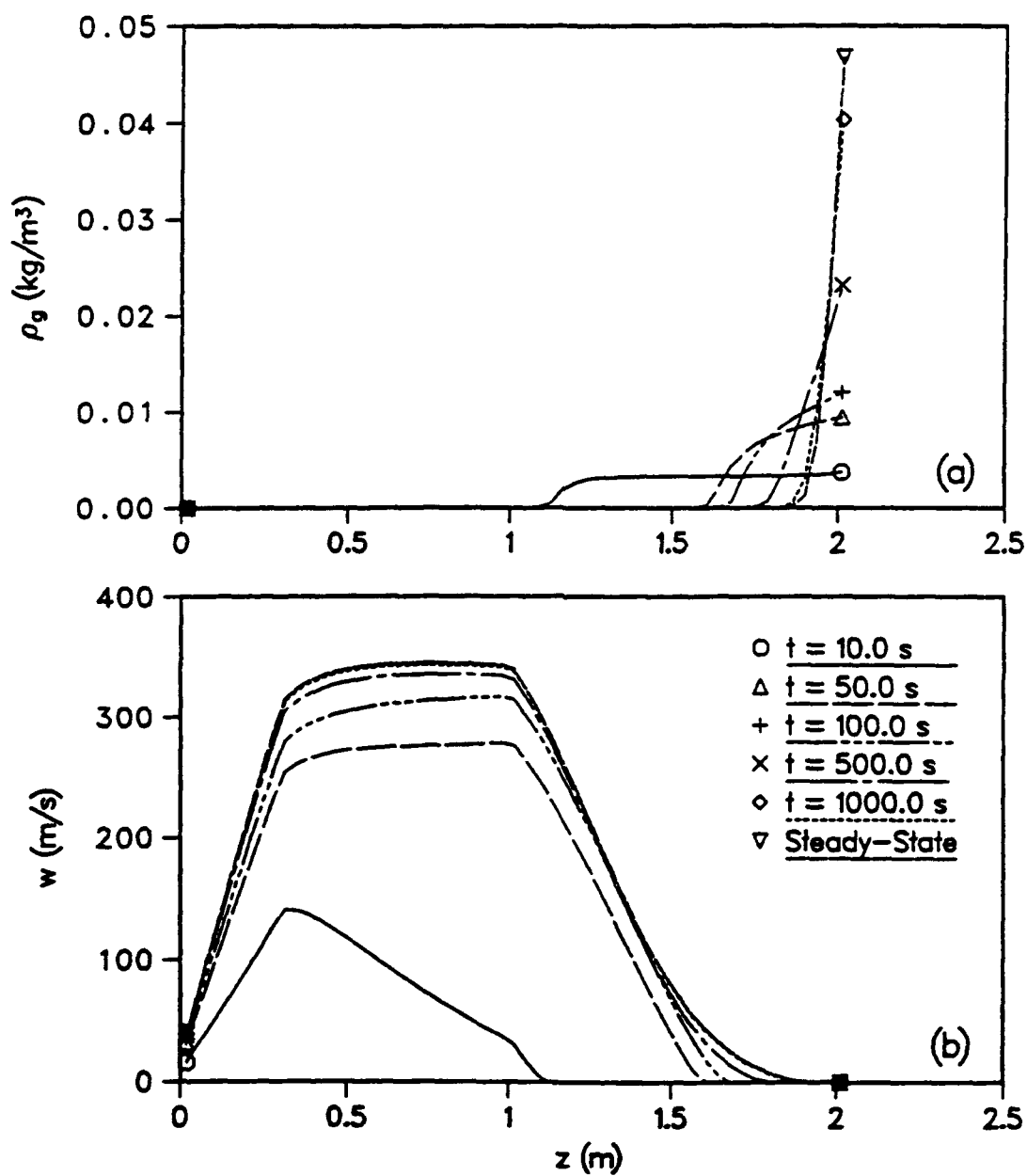


Figure 3.6: Vapor-gas dynamics for the gas-loaded heat pipe with $Q_{in} = 451$ W (Case 2): (a) Transient centerline gas density profile; (b) Transient centerline axial velocity profile.

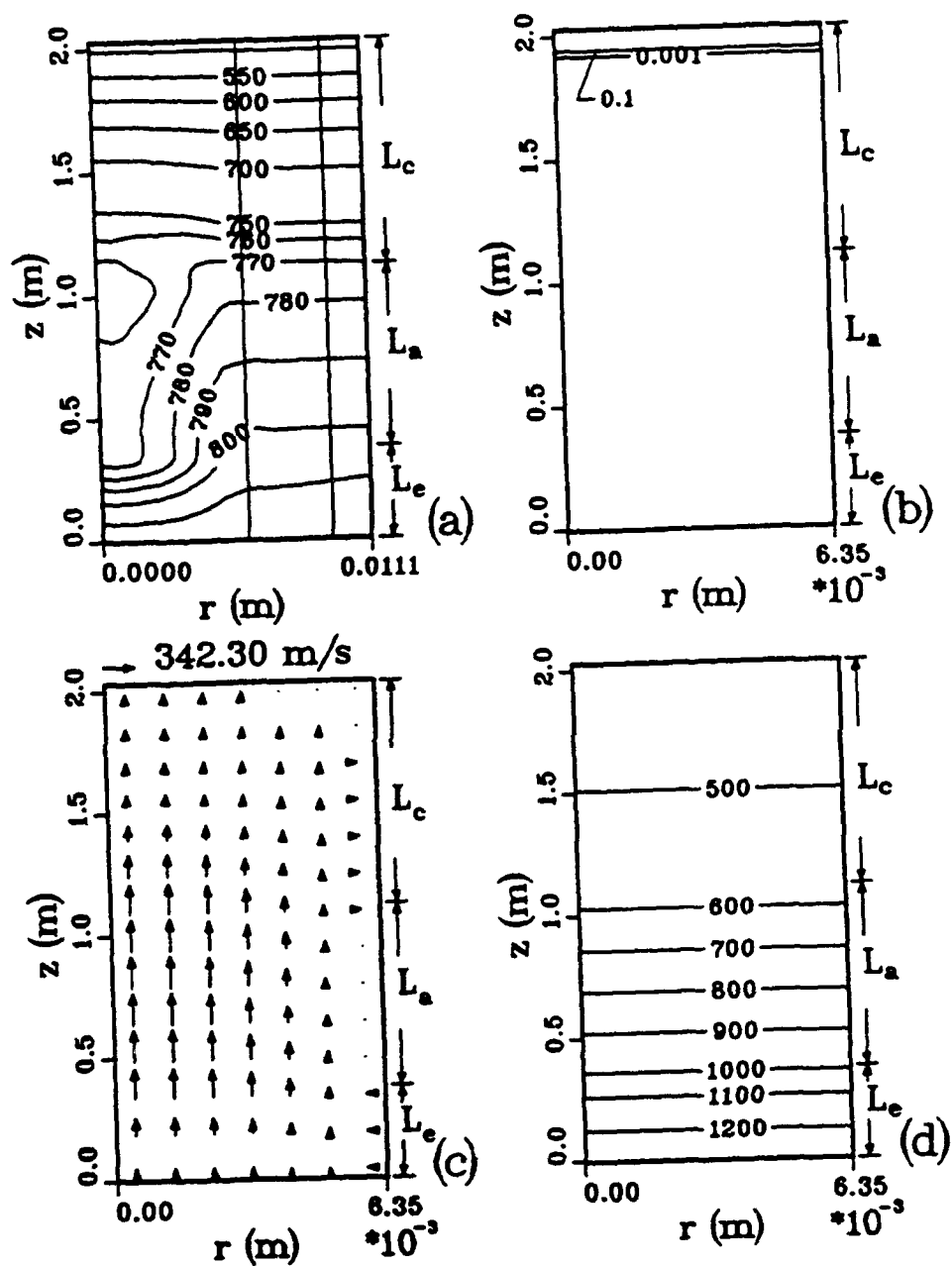


Figure 3.7: Numerical simulation of the gas-loaded high-temperature heat pipe (Case 3): (a) Vapor temperature contours; (b) Noncondensable gas density profiles; (c) Vapor velocity vectors in the r - z plane; (d) Vapor pressure contours.

inactive condenser section.

The vapor density contours, shown in Fig. 3.7(b), are radially uniform and have a sharp axial gradient. This is a conduction-controlled heat pipe, with axial conduction through the heat pipe wall and wick as the principal heat transfer mechanism across the vapor-gas interface.

The results for Case 3 with a heat input of 258 W are shown in Figs. 3.8 and 3.9. In Fig. 3.8(a), the steady-state wall temperature is compared with the experimental data by Ponnappan (1989) with reasonable agreement. In Fig. 3.9(a), the transient gas density profiles are given, where the importance of including conjugate heat transfer with the wall can be recognized. If the gas distribution were controlled purely by the vapor dynamics, the transient time would be on the order of 10^{-3} s (Shukla, 1981). Due to the presence and subsequent damping effect of the wall, the transient time of the noncondensable gas distribution is substantially increased. Physically, this phenomenon is controlled by temperature-dependent diffusion. At the beginning of operation, after liquid- or solid-state startup, the vapor temperature in the condenser is high. This high temperature increases the diffusive mass flux across the vapor-gas interface. However, as time increases, the vapor temperature in the condenser decreases, thus decreasing the mass flux of the noncondensable gas across the interface, and increasing the partial gas density in the reservoir. This phenomenon is reinforced by the compressible behavior of the vapor. As shown in

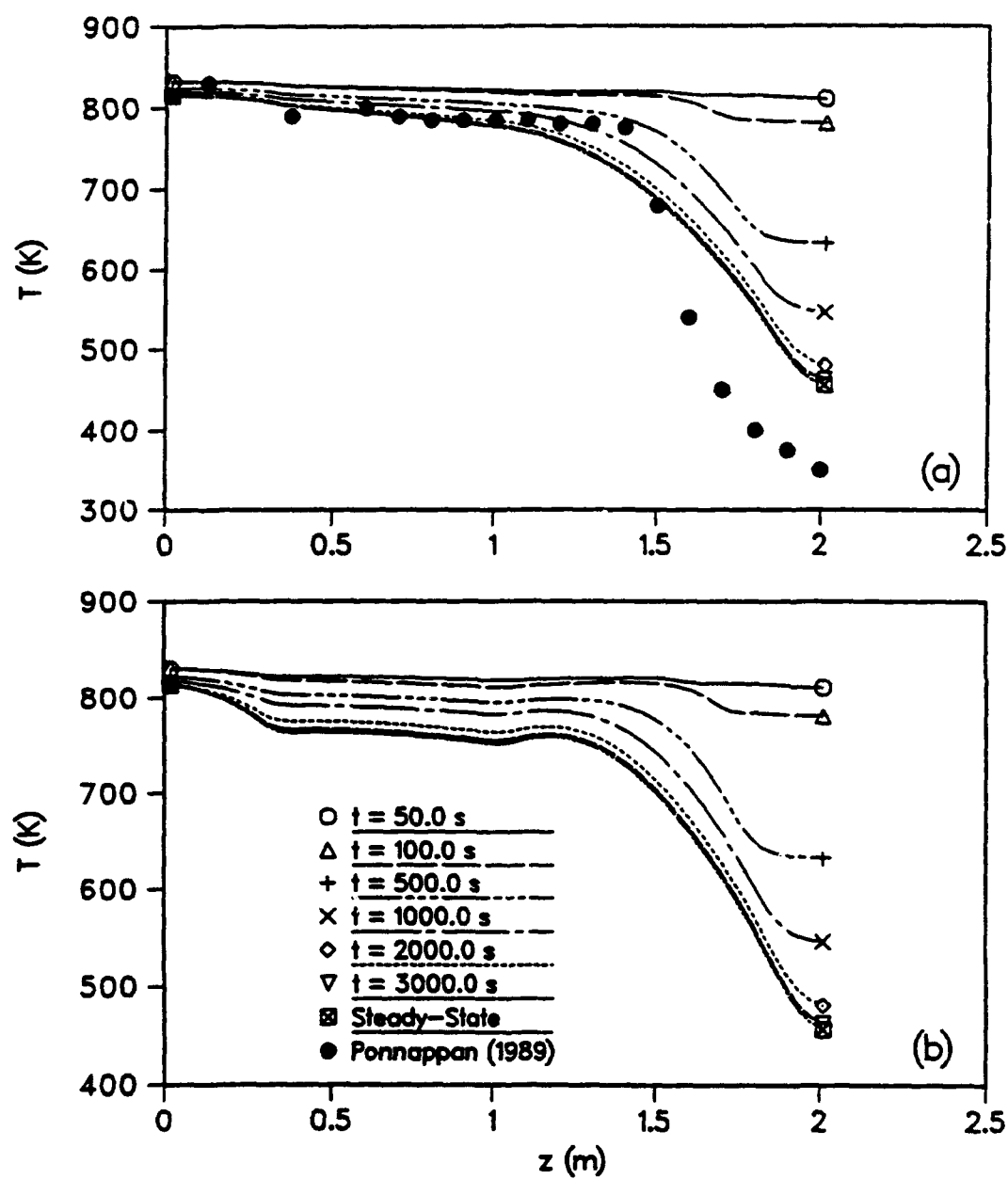


Figure 3.8: Temperature profiles for the gas-loaded heat pipe with $Q_{in} = 258$ W (Case 3): (a) Transient wall temperature profile; (b) Transient centerline temperature profile.

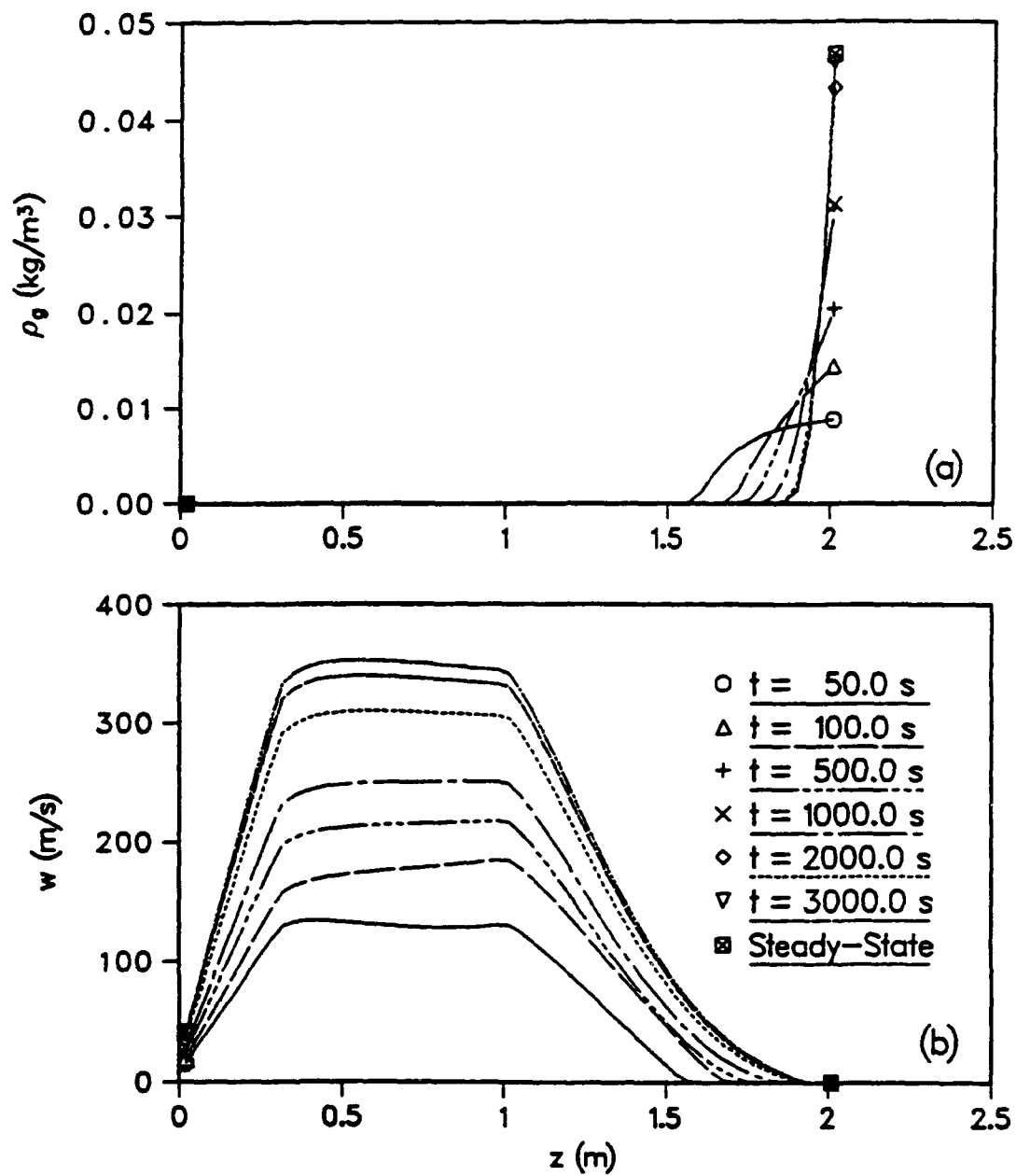


Figure 3.9: Vapor-gas dynamics for the gas loaded heat pipe with $Q_{in} = 258$ W (Case 3): (a) Transient centerline gas density profile; (b) Transient centerline axial velocity profile.

Fig. 3.9(b), the vapor velocity is initially low. Therefore, the inertial effects of the vapor against the stationary noncondensable gas are small. As time increases, the vapor temperature increases in the evaporator, causing the vapor density to decrease. Thus, to maintain the same mass flow rate, the vapor velocity must increase. This velocity increase causes an increase in the inertial forces acting on the noncondensable gas, which further compresses the gas slug.

After the gas-loaded heat pipe reached the steady state for a heat input of 258 W, the heat input was pulsed to 306 W, as shown in Figs. 3.10 and 3.11. The transient axial temperature profiles are shown in Fig. 3.10, and the transient vapor-gas dynamics are shown in Fig. 3.11. The curves labeled with $t = 0.0$ s. are corresponding to the steady state for $Q_{in} = 258$ W. Of primary concern in Fig. 3.10 is the comparison of the transient time for the 258 to 306 W heat pulse with that of the initial response to the 258 W heat input. As expected, the pulsed transient time is nearly 30% of the initial response time. Physically, this is due to the conduction-controlled behavior of the heat pipe. In the initial 258 W response, the heat stored in the condenser pipe wall needed to be rejected to the ambient as the noncondensable gas plug developed. However, at the application of the 258 to 306 W heat pulse, the condenser temperature was much closer to its final value, which required much less time to adjust.

As the operating power changed from 258 to 306 W, the vapor pressure

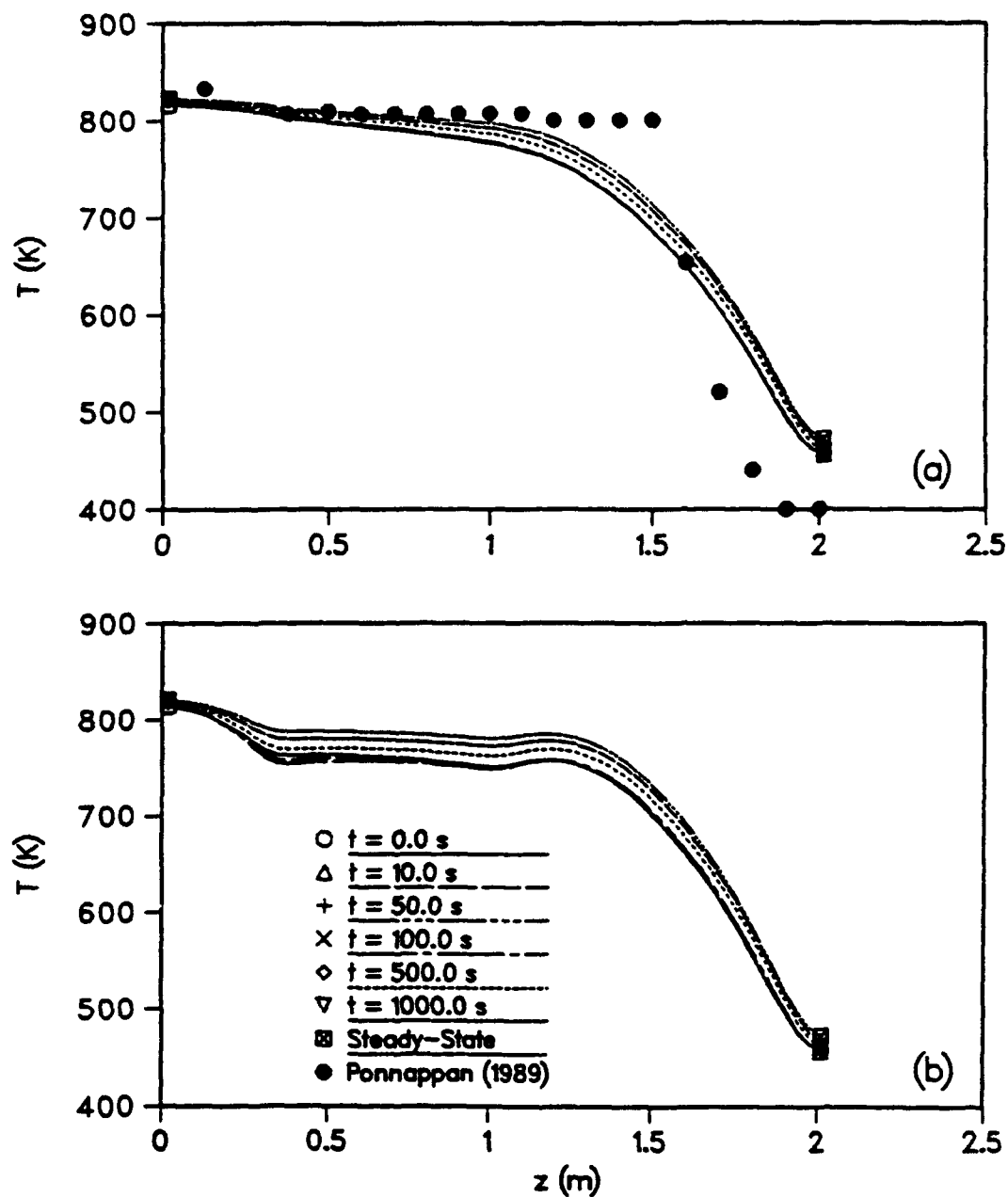


Figure 3.10: Temperature profiles for the gas-loaded heat pipe with a pulsed heat input of $Q_{in} = 258$ to 306 W (Case 3): (a) Transient wall temperature profile; (b) Transient centerline temperature profile.

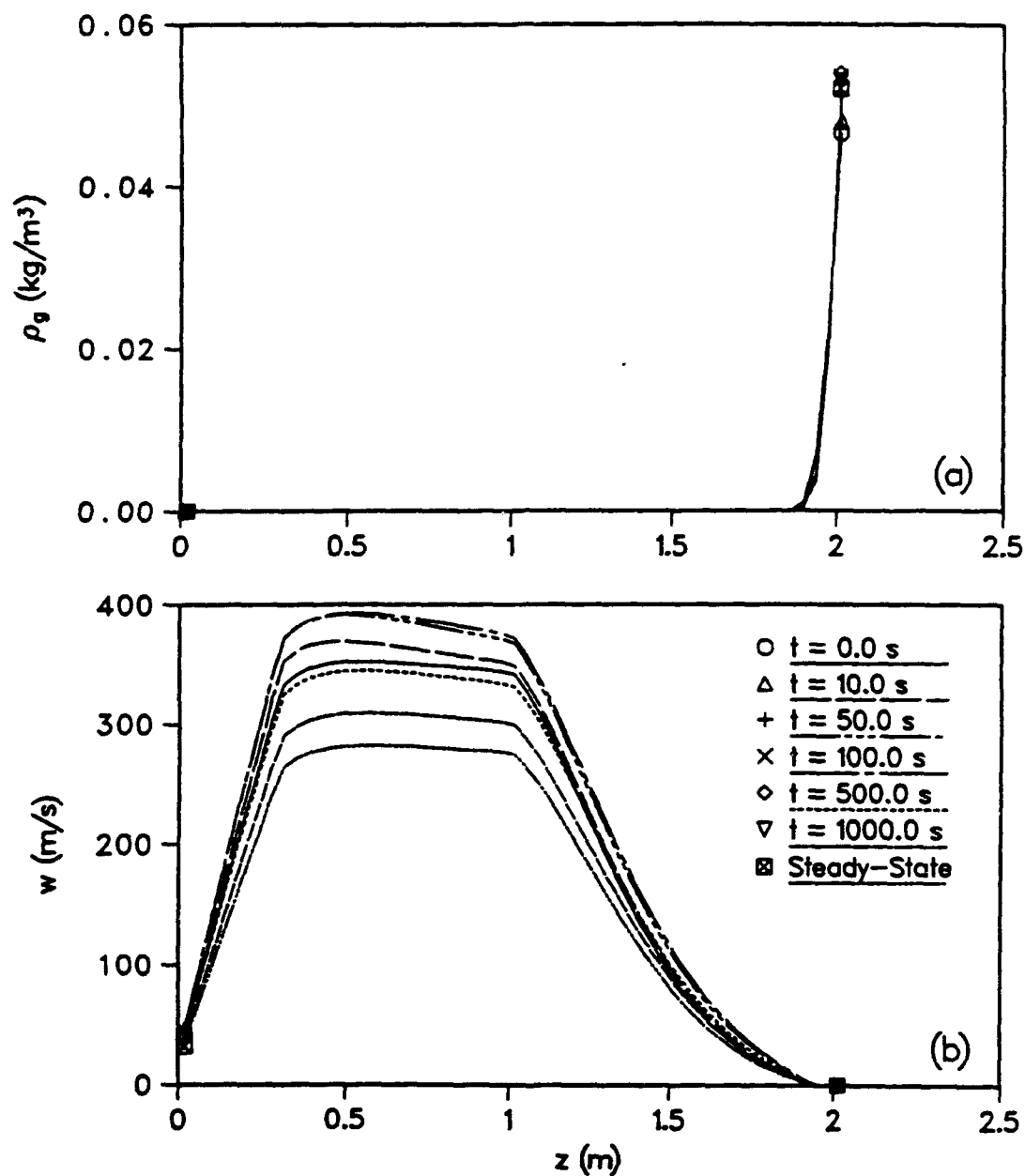


Figure 3.11: Vapor-gas dynamics for the gas-loaded heat pipe with a pulsed heat input of $Q_{in} = 258$ to 306 W (Case 3): (a) Transient centerline gas density profile; (b) Transient centerline axial velocity profile.

of the heat pipe increased. This pressure increase compressed the noncondensable gas plug, and increased the active condenser length, as can be seen in Fig. 3.11(a). However, this pressure increase caused the vapor density to increase, due to the vapor compressible effects. As the density increased, the vapor velocity decreased to maintain a constant mass flow rate. As before, these compressibility effects can be seen in Fig. 3.11(b).

The transient axial temperature results for a pulsed heat input of 258 to 451 W (Case 4) are shown in Fig. 3.12, and the vapor-gas dynamics are shown in Fig. 3.13. The main factor to be examined from this case is the initial response of the gas-loaded heat pipe, as shown in Figs. 3.12(b) and 3.13(b). As the heat input is pulsed from 258 to 451 W, the vapor temperature initially dropped at the inlet to the adiabatic section. Similarly, the axial velocity at that point increased nearly 60%. These effects have been observed by Cao and Faghri (1990) and are attributed to compressibility effects.

3.6 CONCLUSIONS

A transient two-dimensional simulation of gas-loaded heat pipes has been performed. The present numerical model used a conjugate solution technique to couple the unsteady heat transfer in the wall and wick with the transient vapor flow. The boundary condition at the outer condenser pipe wall influenced the operating temperature of

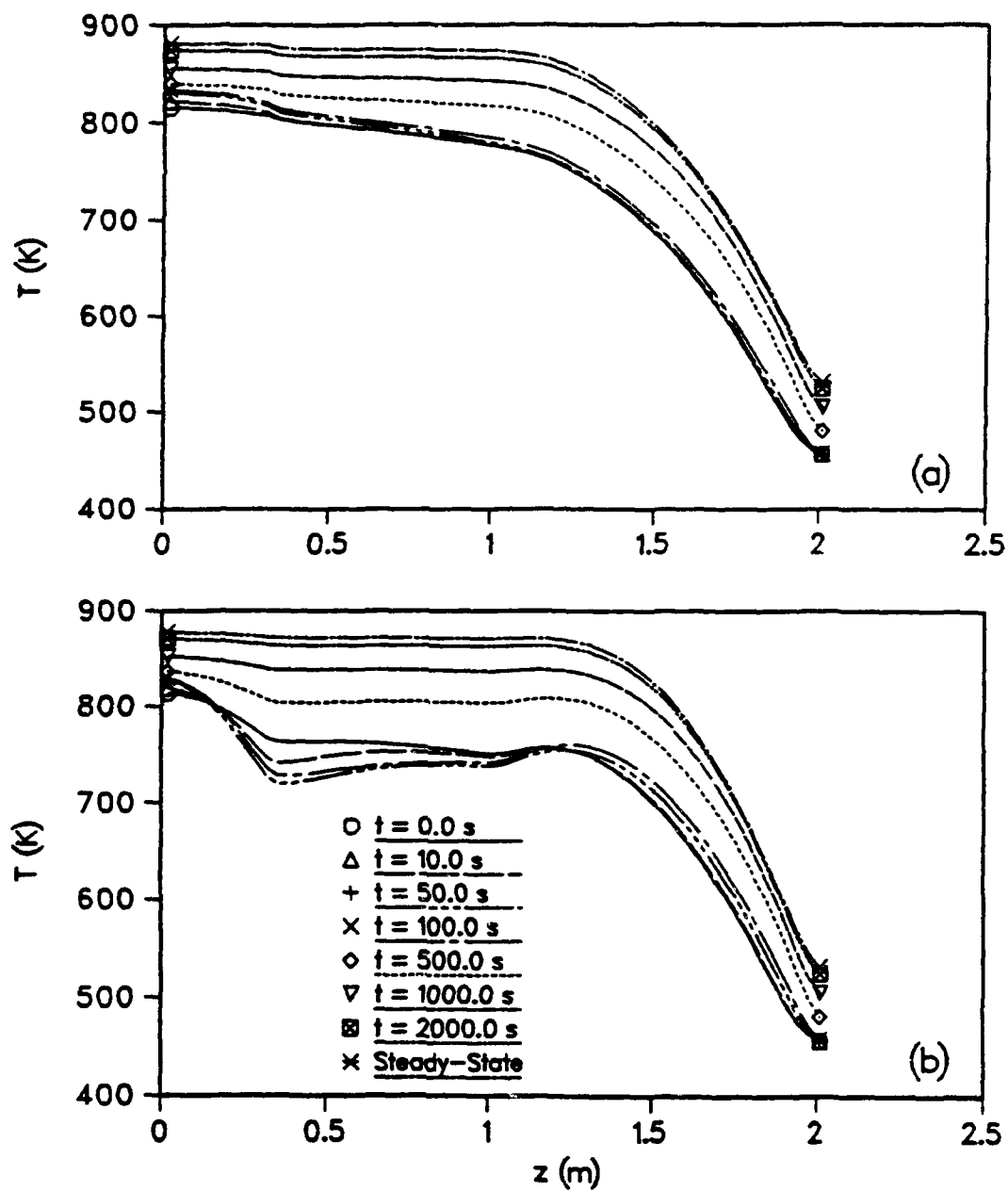


Figure 3.12: Temperature profiles for the gas-loaded heat pipe with a pulsed heat input of $Q_{in} = 258$ to 451 W (Case 4): (a) Transient wall temperature profile; (b) Transient centerline temperature profile.

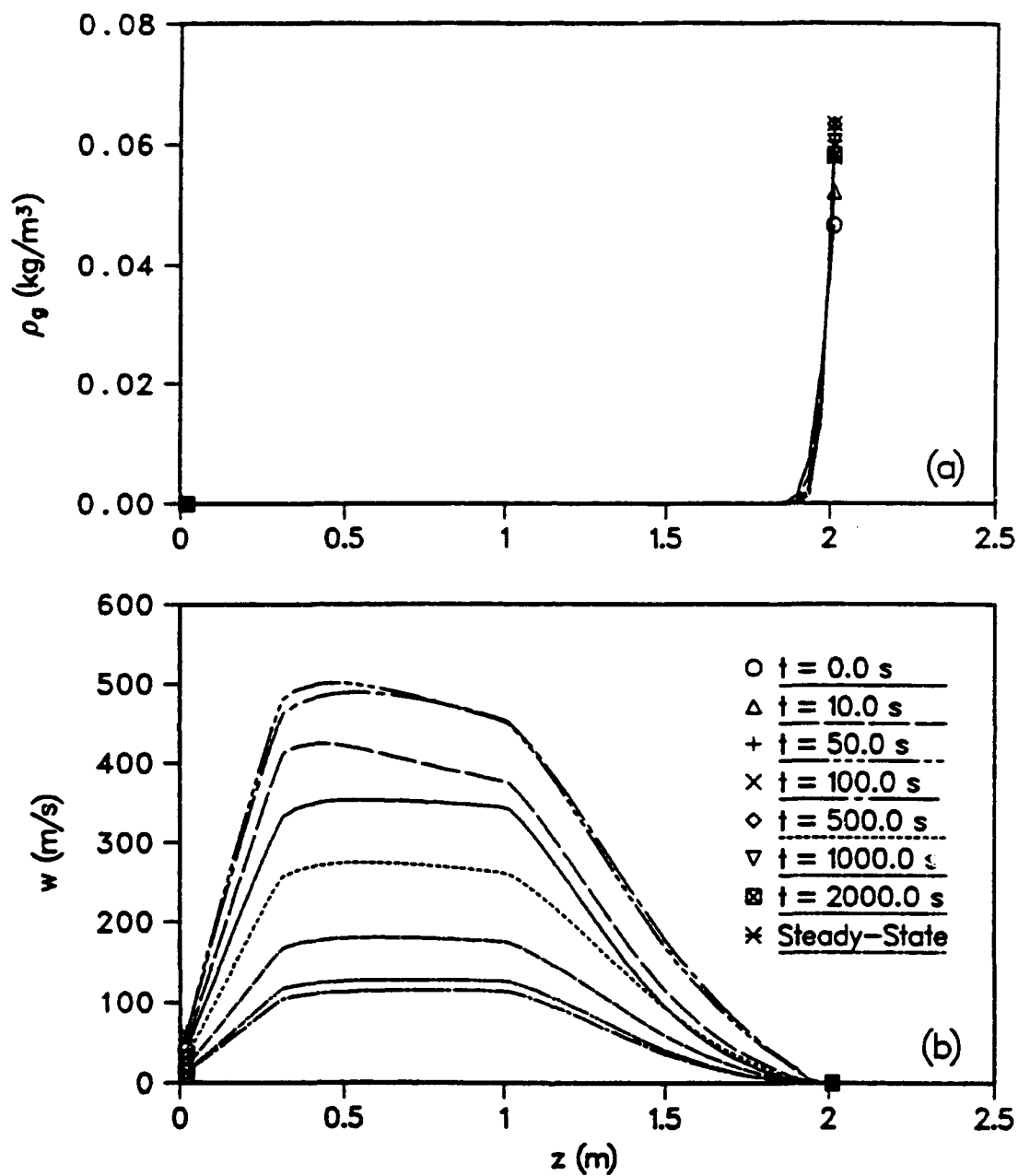


Figure 3.13: Vapor-gas dynamics for the gas-loaded heat pipe with a pulsed heat input of $Q_{in} = 258$ to 451 W (Case 4): (a) Transient centerline gas density profile; (b) Transient centerline axial velocity profile.

the heat pipe and altered the position of the vapor-gas interface. Increasing the radiant emissivity decreased the operating temperature and transient time period of the heat pipe. Steady-state gas-loaded heat pipe operation depends heavily on the mass of noncondensable gas, as this parameter affects the operating temperature and active condenser length. It was also shown that the transient time period increased when gas was added because more heat needed be conducted through the pipe wall to the previously active part of the condenser section. While the noncondensable gas is fundamentally one-dimensional in nature, the complete problem must be solved in two dimensions accounting for conjugate heat transfer through the wall and wick.

REFERENCES

R.B. Bird, W.E. Stewart and E.N. Lightfoot, 1960, *Transport Phenomena*, Wiley, New York.

W.J. Bowman and J. Hitchcock, 1989, "Transient, compressible heat pipe vapor dynamics," *Proc. 25th ASME National Heat Transfer Conf.*, Houston, TX, pp. 329-337.

W.J. Bowman, 1987, "Simulated Heat Pipe Vapor Dynamics," Ph.D. Dissertation, Air Force Institute of Technology, Dayton, OH.

C.A. Busse, 1967, "Pressure Drop in the Vapor Phase of Long Heat Pipes," *Proc. Thermionics Conversion Specialist Conf.*, Palo Alto, CA, pp. 391-398.

C.J. Camarda, 1988, "Thermostructural Applications of Heat Pipes for High-speed Aerospace Vehicles," *Proc. 3rd Int. Heat Pipe Symp.*, Tsukuba, Japan, pp. 31-43.

C.J. Camarda, 1977, "Analysis and Radiant Heating Tests of a Heat-pipe-cooled Leading Edge," NASA TN-8486.

Y. Cao and A. Faghri, 1990a, "Transient Two-Dimensional Compressible Analysis for High-Temperature Heat Pipes With Pulsed Heat Input," *Numerical Heat Transfer*, Part A, Vol. 18, pp. 483-502.

Y. Cao and A. Faghri, 1990b, "A Numerical Analysis of Phase-change Problems Including Natural Convection," *ASME J. Heat Transfer*, Vol. 112, pp. 812-816.

References

Y. Cao and A. Faghri, 1991, "Transient Multidimensional Analysis of Non-conventional Heat Pipes With Uniform and Nonuniform Heat Distributions," *ASME J. Heat Transfer*, Vol. 113, pp. 995-1000.

Y. Cao and A. Faghri, 1992, "Closed-form Analytical Solutions of High-temperature Heat Pipe Startup and Frozen Startup Limitation," *ASME J. Heat Transfer*, Vol. 114, pp. 1028-1035.

Y. Cao and A. Faghri, 1993a, "A Numerical Analysis of High-temperature Heat Pipe Startup from the Frozen State," *ASME J. Heat Transfer*, Vol. 115, pp. 247-254.

Y. Cao and A. Faghri, 1993b, "Simulation of the Early Startup Period of High-temperature Heat Pipes from the Frozen State by a Rarefied Vapor Self-diffusion Model," *ASME J. Heat Transfer*, Vol. 115, pp. 239-246.

Y. Cao and A. Faghri, 1993, "A Numerical Analysis of High Temperature Heat Pipe Startup From the Frozen State," *ASME J. Heat Transfer*, Vol. 115, pp. 239-246.

Y. Cao and A. Faghri, 1990, "Transient Two-dimensional Compressible Analysis for High-Temperature Heat Pipes with Pulsed Heat Input," *Numerical Heat Transfer*, Part A, Vol. 18, pp. 483-502.

W.S. Chang and G.T. Colwell, 1985, "Mathematical Modeling of the Transient Operating Characteristics of a Low-temperature Heat Pipe," *Numer. Heat*

References

Transfer, Vol. 8, pp. 169-186.

S.W. Chi, 1976, *Heat Pipe Theory and Practice: A Sourcebook*, Hemisphere, Washington, D.C.

F.A. Costello, et al., 1987, "Detailed Transient Model of a Liquid-metal Heat Pipe," *Trans. 4th Symp. Space Nuclear Power Systems*, CONF-870102-Summs, Albuquerque, NM.

T.P. Cotter, 1967, "Heat Pipe Start-up Dynamics," *Proc. Thermionics Conversion Specialist Conf.*, Palo Alto, CA.

J.E. Deverall, J.E. Kemme and L.W. Florschuetz, 1970, "Sonic Limitations and Startup Problems of Heat Pipes," Los Alamos Scientific Laboratory Report No. LA-4518, Los Alamos, NM.

P.D. Dunn and D.A. Reay, 1982, *Heat Pipes*, 3rd ed., Pergamon Press, New York.

D.K. Edwards, V.E. Denny and A.F. Mills, 1979, *Transfer Processes: An Introduction to Diffusion, Convection, and Radiation*, Hemisphere, New York.

D.K. Edwards and B.D. Marcus, 1972, "Heat and Mass Transfer in the Vicinity of the Vapor-Gas Front in a Gas-Loaded Heat Pipe," *ASME J. Heat Transfer*, Vol. 94, pp. 155-162.

A. Faghri, 1992, "Frozen startup behavior of low-temperature heat pipes," *Int. J. Heat Mass Transfer*, Vol. 35, pp. 1681-1694.

References

A. Faghri, M. Buchko and Y. Cao, 1991a, "A Study of High-Temperature Heat Pipes With Multiple Heat Sources and Sinks: Part I — Experimental Methodology and Frozen Startup Profiles," *ASME J. Heat Transfer*, Vol. 113, pp. 1003-1009.

A. Faghri, M. Buchko and Y. Cao, 1991b, "A Study of High-Temperature Heat Pipes With Multiple Heat Sources and Sinks: Part II — Analysis of Continuum Transient and Steady-State Experimental Data With Numerical Predictions," *ASME J. Heat Transfer*, Vol. 113, pp. 1010-1016.

A. Faghri and C. Harley, 1993, "Transient Lumped Heat Pipe Analysis," *Heat Recovery Systems and CHP* (in press).

E.N. Ganic, J.P. Hartnett and W.M. Rohsenow, 1985, "Basic Concepts of Heat Transfer," in *Handbook of Heat Transfer Fundamentals*, Rohsenow, W.M., et al. (eds.), McGraw-Hill, New York.

M.L. Hall and J.M. Doster, 1990, "A Sensitivity Study of the Effects of Evaporation/condensation Accommodation Coefficients on Transient Heat Pipe Modeling," *Int. J. Heat Mass Transfer*, Vol. 33, pp. 465-481.

C. Harley and A. Faghri, 1993, "Transient Two-Dimensional Gas-Loaded Heat Pipe Analysis," *ASME J. Heat Transfer* (in press).

J.O. Hirschfelder, C.F. Curtiss and R.B. Bird, 1966, *Molecular Theory of Gases and Liquids*, Wiley, New York.

M.N. Ivanovskii, V.P. Sorokin and I.V. Yagodkin, 1982, *The Physical Prin-*

References

ciples of Heat Pipes, Clarendon Press, Oxford.

J.H. Jang, A. Faghri, W.S. Chang and E.T. Mahefkey, 1990, "Mathematical Modeling and Analysis of Heat Pipe Startup from the Frozen State," *ASME J. Heat Transfer*, Vol. 112, pp. 586-594.

J.H. Jang, A. Faghri and W.S. Chang, 1991, "Analysis of the One-dimensional Transient Compressible Vapor Flow in Heat Pipes," *Int. J. Heat Mass Transfer*, Vol. 34, pp. 2029-2037.

B.D. Marcus and G.L. Fleischman, 1970, "Steady State and Transient Performance of Hot Reservoir Gas-Controlled Heat Pipes," ASME Paper No. 70-HT/SpT-11, 1970.

M.A. Merrigan, E.S. Keddy and J.T. Sena, 1986, "Transient Performance Investigation of a Space Power System Heat Pipe," AIAA Paper No. 86-1273.

S.V. Patankar, 1980, *Numerical Heat Transfer and Fluid Flow*, Hemisphere, Washington, D.C.

S.V. Patankar, 1988, "Elliptic Systems: Finite-Difference Method I," in *Handbook of Numerical Heat Transfer*, W.J. Minkowycz et al., eds., Wiley, New York.

R. Ponnappan, 1989, "Studies on the Startup Transients and Performance of a Gas-loaded Sodium Heat Pipe," Technical Report, WRDC-TR-89-2046, Universal Energy Systems, Inc., Dayton, OH.

R. Ponnappan, 1989, "Studies on the Startup Transients and Performance

References

of a Gas Loaded Sodium Heat Pipe," WRDC-TR-89-2046, Wright Patterson AFB, OH.

A.R. Rohani and C.L. Tien, 1973, "Steady Two-Dimensional Heat and Mass Transfer in the Vapor-Gas Region of a Gas-Loaded Heat Pipe," *ASME J. Heat Transfer*, Vol. 95, pp. 377-382.

K.N. Shukla, 1981, "Transient Response of a Gas-Controlled Heat Pipe," *AIAA Journal*, Vol. 19, No. 8, pp. 1063-1070.

R.S. Silver and H.C. Simpson, 1961, "The Condensation of Superheated Steam," *Proc. National Engineering Laboratory Conf.*, Glasgow, Scotland.

P.M. Sockol and R. Forman, 1970, "Re-examination of Heat Pipe Startup," *Proc. 9th IEEE Thermionic Conversion Specialist Conf.*, pp. 571-573.

S.P. Sukhatme and W.M. Rohsenow, 1966, "Heat Transfer during Film Condensation of a Liquid Metal Vapor," *ASME J. Heat Transfer*, pp. 19-28.

C.L. Tien and J.H. Lienhard, 1979, *Statistical Thermodynamics*, Hemisphere, New York.

W.E. Wageman and F.A. Guevara, 1960, "Fluid Flow Through a Porous Channel," *Physics Fluids*, Vol. 3, pp. 878-881.

S.W. Yuan and A.B. Finkelstein, 1956, "Laminar Pipe Flow with Injection and Suction Through a Porous Wall," *Transactions of the ASME*, pp. 719-724.